Journal of Cerebral Blood Flow & Metabolism (2009), 1–11

www.jcbfm.com

# Measurement of density and affinity for dopamine $D_2$ receptors by a single positron emission tomography scan with multiple injections of [$^{11}$C]raclopride

Yoko Ikoma[1,2], Hiroshi Watabe[1], Takuya Hayashi[1], Yoshinori Miyake[1], Noboru Teramoto[1], Kotaro Minato[2] and Hidehiro Iida[1]

[1]*Department of Investigative Radiology, National Cardiovascular Center Research Institute, Osaka, Japan;* [2]*Biomedical Imaging and Informatics, Graduate School of Information Science, Nara Institute of Science and Technology, Nara, Japan*

**Positron emission tomography (PET) with [$^{11}$C]raclopride has been used to investigate the density ($B_{max}$) and affinity ($K_d$) of dopamine $D_2$ receptors related to several neurological and psychiatric disorders. However, in assessing the $B_{max}$ and $K_d$, multiple PET scans are necessary under variable specific activities of administered [$^{11}$C]raclopride, resulting in a long study period and unexpected physiological variations. In this paper, we have developed a method of multiple-injection graphical analysis (MI-GA) that provides the $B_{max}$ and $K_d$ values from a single PET scan with three sequential injections of [$^{11}$C]raclopride, and we validated the proposed method by performing numerous simulations and PET studies on monkeys. In the simulations, the three-injection protocol was designed according to prior knowledge of the receptor kinetics, and the errors of $B_{max}$ and $K_d$ estimated by MI-GA were analyzed. Simulations showed that our method could support the calculation of $B_{max}$ and $K_d$, despite a slight overestimation compared with the true magnitudes. In monkey studies, we could calculate the $B_{max}$ and $K_d$ of diseased or normal striatum in a 150 mins scan with the three-injection protocol of [$^{11}$C]raclopride. Estimated $B_{max}$ and $K_d$ values of $D_2$ receptors in normal or partially dopamine-depleted striatum were comparable to the previously reported values.**

*Journal of Cerebral Blood Flow & Metabolism* advance online publication, 11 November 2009; doi:10.1038/jcbfm.2009.239

**Keywords:** [$^{11}$C]raclopride; dopamine $D_2$ receptors; graphical analysis; multiple injections; positron emission tomography

## Introduction

Positron emission tomography (PET) with [$^{11}$C]raclopride has been widely used to investigate the availability of striatal dopamine $D_2$ receptors *in vivo* (Farde *et al*, 1985; Köhler *et al*, 1985; Hall *et al*, 1988). A number of postmortem studies have shown that the abundance of dopamine $D_2$ receptor is elevated in striatum samples from untreated patients with Parkinson's disease (Guttman and Seeman, 1985; Seeman *et al*, 1987) and in schizophrenic patients who had never taken antipsychotics (Cross *et al*, 1981; Joyce *et al*, 1988). The PET measurements have made it possible to quantify *in vivo* the density and apparent affinity of receptors by systematically varying the specific activity (or mass) of an administered radioligand (see for example, Farde *et al*, 1986). A study of Parkinson's disease by Rinne *et al* (1995) with *in vivo* PET showed increased density and unchanged affinity of dopamine $D_2$ receptors in the putamen in comparison with healthy controls. In corresponding studies of schizophrenia, early findings with [$^{11}$C]*N*-methylspiperone indicated elevated $D_2$ binding, which was not replicated in some subsequent studies with [$^{11}$C]raclopride (Wong *et al*, 1986; Farde *et al*, 1987, 1990). Dysfunction of dopamine receptors has also been suggested in other neurodegenerative or psychiatric diseases (e.g., multiple-system atrophy, progressive supranuclear palsy, and attention-deficit hyperactivity disorders); however, there have been only a few studies that

Correspondence: Dr H Watabe, Department of Investigative Radiology, National Cardiovascular Center Research Institute, 5-7-1, Fujishirodai, Suita, Osaka 565-8565, Japan.
E-mail: watabe@ri.ncvc.go.jp
Received 11 September 2009; revised 13 October 2009; accepted 19 October 2009

examined receptor function directly related to density and affinity. This might be due to the inherent difficulty in measuring absolute receptor abundance based on PET recordings.

In PET scans, to determine the density and affinity of receptors directly as parameters of kinetic model, it is necessary to apply a compartmental analysis based on a two-tissue compartment five-parameter model including density of receptors $B_{max}$ (pmol/mL), bimolecular association rate constant $k_{on}$ (mL/pmol/min), and unimolecular dissociation rate constant $k_{off}$ ($min^{-1}$) (Farde *et al*, 1989). However, since data from a single PET scan are not enough to determine the $B_{max}$ and $k_{on}$ individually, multiple PET scans should be taken with different molar amounts of injected ligand. In addition, model parameters are estimated by a nonlinear least squares fitting with the metabolite-corrected plasma input function, so the solutions are often unstable and sensitive to statistical noise, and invasive arterial sampling is required to use this method.

Farde *et al* (1986, 1989) determined the value of $B_{max}$ and apparent affinity $K_d$ ($=k_{off}/k_{on}$) by a graphical analysis using a time-activity curve (TAC) of the specifically bound target region and a reference region where specific bindings are negligible. In this method, the ratio of specific bound and free ligand concentrations at the equilibrium state are plotted versus the concentration of specific bound ligand, and $B_{max}$ and $K_d$ are estimated from the slope and intercept of the regression line. Other groups also used the value of distribution volume ratio − 1 estimated from the graphical analysis of Logan *et al* (1996), instead of the ratios of specific bound and free concentration, to obtain stable values of the *y*-axis quantity (Logan *et al*, 1997; Doudet and Holden, 2003; Doudet *et al*, 2003). These methods are practical, because they do not require arterial blood sampling, and their respective estimation processes are easy to carry out. However, to estimate the regression line of a graphical plot, multiple PET scans (at least two or three) are required under variable molar amounts of administered ligand, so scans have been performed on separate days. Even in quantitative PET scans, the separate day protocol may suffer from interday or intraday variations in physiologic conditions, such as cerebral blood pressure, flow, and receptor bindings, which may affect the accuracy of the estimates.

We developed a method, called the multiple-injection simplified reference tissue model (MI-SRTM), to measure the change in binding potential ($BP_{ND}=k_3/k_4$ (Mintun *et al*, 1984)) of dopamine $D_2$ receptors from a single session of PET scanning with multiple injections of [$^{11}$C]raclopride (Watabe *et al*, 2006; Ikoma *et al*, 2009), and we showed that this method could detect the change in $BP_{ND}$ because of an increase in mass of administered [$^{11}$C]raclopride in a short scanning period, which is a prerequisite for measuring the saturation binding parameters as steady state. In this study, we extend our earlier report for estimating $B_{max}$ and $K_d$ from a single session of PET scanning with triple injections of [$^{11}$C]raclopride using MI-SRTM and the graphical analysis, and we validated the proposed method by performing numerous simulations and studies on monkeys using PET and [$^{11}$C]raclopride.

## Materials and methods

### Theory

*Graphical Analysis with a Reference Region for Estimation of Density and Affinity*: Graphical analysis based on the Scatchard plot (Scatchard, 1949) has been used to estimate the values of $B_{max}$ and $K_d$ from as series of PET recordings with various molar amounts of administered ligand (Farde *et al*, 1986). In brief, the ratios ($B/F$) of specific bound ligand concentration ($B$ [pmol/mL]) and free ligand concentration ($F$ [pmol/mL]) at equilibrium are plotted versus $B$. In this plot, the slope and *x*-intercept represent $-1/K_d$ and $B_{max}$, respectively. In general, for graphical analysis without arterial blood sampling, the total radioligand concentration in the reference region ($C_r$ [Bq/mL]), where specific bindings are negligible, is used as an estimate of the free radioligand concentration in the target region ($C_t$ [Bq/mL]), that is $C_f^{ref}=C_r$, and the specific binding radioligand concentration in the target region ($C_b$ [Bq/mL]) is defined as radioactivity in the target region ($C_t$ [Bq/mL]) reduced with $C_r$, that is $C_b^{ref}=C_t-C_r$ (Figure 1). The radioactivity concentrations of $C_f^{ref}$ and $C_b^{ref}$, at the point in time when $dC_b^{ref}/dt$ is 0 ($T_{eq}$), are divided by a specific activity of the administered ligand, and used as $F$ and $B$ at the transient equilibrium in the graphical analysis

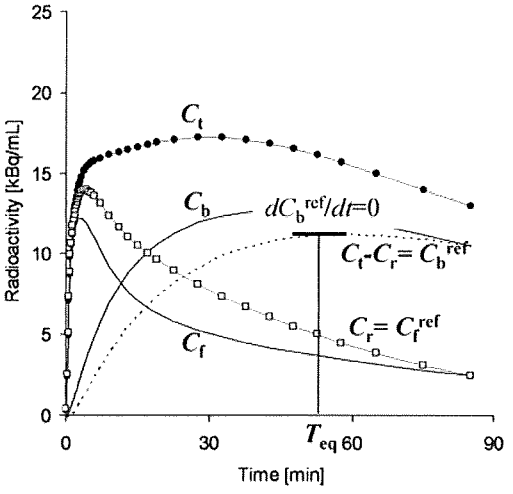


**Figure 1** An example of simulated TACs for the striatum ($C_t$), free ($C_f$), and specific bound ($C_b$) concentrations in the striatum, the cerebellum used as a reference region ($C_r$) and bound concentration in the striatum estimated using a reference region ($C_b^{ref}=C_t-C_r$) with $K_1=0.033$, $K_1/k_2=0.59$, $k_{on}=0.0033$, $B_{max}=25.7$, $k_4=0.034$ for the striatum, and $K_1=0.034$, $K_1/k_2=0.36$, $k_3=0.022$, $k_4=0.034$ for the cerebellum. The time point of $dC_b^{ref}/dt=0$ ($T_{eq}$) is considered the transient equilibrium, and bound concentration at the equilibrium ($B^{ref}$) is obtained from the radioactivity concentration of $C_b^{ref}$ at $T_{eq}$.

(Farde *et al*, 1989). In our study, we use the nomenclature $B^{ref}$ and $F^{ref}$ to represent the concentrations otherwise known as $B$ and $F$. The value of the $y$ axis, $B^{ref}/F^{ref}$, is sometimes replaced by the binding potential estimated by the graphical analysis of Logan *et al* (1996) or some other method (Logan *et al*, 1997; Doudet and Holden, 2003; Doudet *et al*, 2003).

*Multiple-Injection Simplified Reference Tissue Model for Estimation of Binding Potential*: A simplified reference tissue model (SRTM) can provide three parameters ($R_1$, $k_2$, $BP_{ND}$) without invasive arterial blood sampling by using a TAC of the reference region (Lammertsma and Hume, 1996). The MI-SRTM extended this SRTM for sequential multiple injections in a single session of PET scanning by taking into account the residual radioactivity in the target tissue at the time of each injection. As such, the magnitude of $BP_{ND}$ for the $i$th injection is described in the following terms (Ikoma *et al*, 2009):

$$C_{ti}(t) = R_{1i}C_{ri}(t) + \left(k_{2i} - \frac{R_{1i}k_{2i}}{1+BP_{NDi}}\right)e^{-\frac{k_{2i}}{1+BP_{NDi}}t} \otimes C_{ri}(t) + (C_{ti}(0) - R_{1i}C_{ri}(0))e^{-\frac{k_{2i}}{1+BP_{NDi}}t} \quad (1)$$

where $C_{ti}$ and $C_{ri}$ are the radioactivity concentrations in the target and reference region, respectively, and $t$ is the time from the start of the $i$th injection.

*Multiple-Injection Graphical Analysis for Estimation of Density and Affinity*: The conventional graphical analysis was applied to the $B_{max}$ and $K_d$ estimations with the multiple-injection approach. In this multiple-injection graphical analysis (MI-GA), the $BP_{ND}$ calculated for each injection using MI-SRTM was plotted as a function of the concentration of specific bound raclopride at the transient equilibrium ($B^{ref}$ [pmol/mL]) within the scan duration for each injection, and $B_{max}$ and $K_d$ were estimated from the regression line.

In this study for [$^{11}$C]raclopride, the TAC of the cerebellum was used as the reference TAC. Each parameter in the MI-SRTM was estimated by nonlinear least squares fitting with iteration of the Gauss–Newton algorithm. It should be noted that the transient equilibrium condition is required for each injection in the MI-GA.

## Simulation Analysis

Simulations were performed to determine the range of administered mass of three injections and to evaluate feasibility of the MI-GA to estimate the $B_{max}$ and $K_d$.

*Effect of Injected Mass on $BP_{ND}$ Estimates*: To investigate the effect of the administered molar amount of [$^{11}$C]raclopride on $BP_{ND}$ estimates and to determine the molar amount of three injections for monkey studies, a relationship between $BP_{ND}$ and $B^{ref}$ was obtained by a computer simulation. Noiseless TACs of the striatum and cerebellum were generated with a measured plasma TAC and assumed parameter values derived from measurements taken from the monkey studies. The TAC of the cerebellum was simulated with a conventional two-tissue compartment four-parameter model with assumed parameter values obtained earlier in our monkey studies: $K_1 = 0.034$ (mL/mL/min) $K_1/k_2 = 0.36$, $k_3 = 0.022$ (min$^{-1}$), $k_4 = 0.034$ (min$^{-1}$). Meanwhile, the TAC of the striatum was simulated with a two-tissue compartment five-parameter model expressed as Equation (2) by solving these differential equations with the numerical analysis of fourth-order Runge–Kutta method with assumed parameter values $K_1 = 0.033$ (mL/mL/min), $K_1/k_2 = 0.59$, $k_{on} = 0.0033$ (mL/pmol/min), $B_{max} = 25.7$ (pmol/mL), $k_4 = 0.026$ (min$^{-1}$), and SA = 37 (GBq/μmol):

$$\begin{aligned} \frac{dC_f}{dt} &= K_1C_p(t) - \left(k_2 + k_3'(t)\right)C_f(t) + k_4C_b(t) \\ \frac{dC_b}{dt} &= k_3'(t)C_f(t) - k_4C_b(t) \\ k_3'(t) &= k_{on}\left(B_{max} - \frac{C_b(t)}{SA}\right) \end{aligned} \quad (2)$$

where $C_f$ and $C_b$ are the concentrations of radioactivity for free and specifically bound [$^{11}$C]raclopride in tissue, respectively; and SA is the specific activity of administered [$^{11}$C]raclopride.

As reference, the relationships between $B^{ref}$ and $BP_{ND}$ or $B^{ref}/F^{ref}$ were investigated in the case of a single injection of [$^{11}$C]raclopride by varying injected mass. TACs of the striatum and cerebellum for the single injection with a 50 mins scan were generated using the measured plasma TAC of a single injection in which the input plasma TAC was amplified, such that the corresponding mass increased from 1 to 500 nmol per injection. In each simulated TAC, $BP_{ND}$ values were estimated by the SRTM, and then, $B^{ref}/F^{ref}$ and $B^{ref}$ were calculated by the transient equilibrium with the cerebellum TAC.

Next, TACs of the striatum and cerebellum for three injections at 50 mins intervals were generated using the plasma TAC of three sequential injections in which the input plasma TAC was amplified so that the mass of the first and second injections would be 1.5 and 10 nmol/kg, and the mass of the third injection would be 1.5 to 150 nmol/kg. In each simulated TAC, $BP_{ND}$ values were estimated by the MI-SRTM, and $B^{ref}/F^{ref}$ and $B^{ref}$ for the third injection was calculated by the transient equilibrium with the cerebellum TAC. The relationships between $B^{ref}$ and $BP_{ND}$ or $B^{ref}/F^{ref}$ for the third injection were investigated, and compared with that for the single injection.

*Estimation of $B_{max}$ and $K_d$ Values by the Multiple-Injection Graphical Analysis*: The reliability of $B_{max}$ and $K_d$ estimates by the graphical analysis was investigated for the proposed sequential multiple-injection approach (single PET scan) and compared with that for the conventional nonsequential approach (three PET scans on different days, such that no residual mass remained). Noiseless TACs of the striatum and cerebellum were simulated using assumed parameters of the two-tissue compartment model mentioned above and the plasma input function for three injections in which the magnitude of each 'virtual' input function was adjusted so that the injection mass would be 1.5, 10, or 30 nmol/kg determined from the simulation study mentioned above, with 50 mins intervals as reported

by Ikoma *et al* (2009). In the striatum TACs, $B_{max}$ values were varied from 10 to 50 pmol/mL at 5 pmol/mL intervals with other parameters fixed ($K_d = 7.9$ pmol/mL), or $K_d$ was varied from 3 to 15 at 2 pmol/mL intervals by changing $k_{on}$ with other parameters fixed ($B_{max} = 25.7$ pmol/mL). For each TAC, $B_{max}$ and $K_d$ were estimated by the MI-GA from three points obtained by MI-SRTM for the single PET scan approach and they were estimated by the graphical analysis from three points obtained by the conventional SRTM for the three PET scan approach. Then, estimates were compared with the true values. In the single PET scan approach, $B_{max}$ and $K_d$ were also estimated without reference TAC by the MI-GA from three points of $BP_{ND}$ and $B$ obtained by the two-tissue compartment four-parameter model with the plasma input function shown in the Appendix.

### Analysis of Monkey Studies

PET studies were performed on three cynomolgus macaques (weight 6.9 ± 2.1 kg) with the multiple-injection approach. One animal (monN) was a healthy monkey aged 5 years, and the others had a syndrome acquired Parkinsonism. Of these, one (monUP, aged 7 years) had hemiparkinsonism induced by injecting the selective neurotoxin, *N*-methyl-4-pheny1-1,2,3,6-tetrahydropyridine (MPTP) (0.4 mg/kg) into the right carotid artery (Bankiewicz *et al*, 1986), whereas the other (monBP, aged 5 years) had bilateral Parkinsonism induced by injecting MPTP (0.4 mg/kg) intravenously and intermittently (twice a week for a total of 14 injections) (Takagi *et al*, 2005). Each Parkinsonian animal showed typical Parkinsonian symptoms in the limbs (motor slowness, tremor) unilaterally or bilaterally. The PET scan was performed after the symptom reaching stable (6 months after the first injection of MPTP). Anesthesia was induced with ketamine (8.4 mg/kg, intramuscularly) and xylazine (1.7 mg/kg, intramuscularly) and maintained by intravenous propofol (6 mg/kg/h) and vecuronium (0.02 mg/kg/h) during the scan. The monkeys were maintained and handled in accordance with guidelines for animal research on Human Care and Use of Laboratory Animals (Rockville, National Institutes of Health/Office for Protection from Research Risks, 1996). The study protocol was approved by the Subcommittee for Laboratory Animal Welfare of the National Cardiovascular Center.

After the synthesis of [$^{11}$C]raclopride, nonradioactive raclopride was added so that targeted molar amount of raclopride would be administered for three injections (1.5, 10, and 30 nmol/kg); this was done by dividing the [$^{11}$C]raclopride diluted by nonradioactive raclopride into three portions with different volumes, containing the intended masses of raclopride. For the first injection, 1.9 ± 0.16 nmol/kg (57.0 ± 5.7 MBq) of [$^{11}$C]raclopride was administered by a bolus injection at the beginning of the scan. Fifty minutes later, the second [$^{11}$C]raclopride injection, 11.1 ± 0.56 nmol/kg (60.4 ± 8.8 MBq at the time of second injection) was administered by a bolus, and 50 mins after that, a bolus of 31.1 ± 2.1 nmol/kg (30.8 ± 4.4 MBq at the time of third injection) of [$^{11}$C]raclopride was administered again. Data were acquired for 150 mins (10 secs × 18, 30 secs × 6, 120 secs × 7, 300 secs × 6; total 50 mins for each injection). The specific radioactivity was 4.7 ± 2.2 GBq/μmol at the time of the first injection.

PET scans were performed using a PCA-2000A positron scanner (Toshiba Medical Systems Corporation, Otawara, Japan) that provides 47 planes and a 16.2 cm axial field-of-view. The transaxial and axial spatial resolution of the PET scanner were 6.3 and 4.7 mm full width at half maximum (Herzog *et al*, 2004). A transmission scan with a 3-rod source of $^{68}$Ge-$^{68}$Ga was performed for 20 mins for attenuation correction before the administration of [$^{11}$C]raclopride. Radioactivity was measured in the three-dimensional mode and the data were reconstructed by a filtered back-projection using a Gaussian filter (3 mm of full width at half maximum). Region-of-interests (ROIs) were defined manually over the left and right striatum and cerebellum for PET images, and the radioactivity concentrations in these regions were obtained. For the left and right striatum, $R_1$, $k_2$, and $BP_{ND}$ for each injection were estimated by the MI-SRTM. In addition, parametric images were generated, estimating each parameter voxel by voxel, using the MI-SRTM with a basis function method in which the model Equation (1) was solved using linear least squares for a set of basis functions, which enables the incorporation of parameter bounds (Gunn *et al*, 1997; Ikoma *et al*, 2009). $B_{max}$ and $K_d$ were estimated by the MI-GA from these $BP_{ND}$ values of left and right striatum for three injections.

In the unilateral Parkinsonian animal, three PET scans with conventional single injection with different masses of [$^{11}$C]raclopride were also performed for comparison with results by the multiple-injection single PET scan approach. A PET scan with a bolus injection of 2.1 nmol/kg (50.6 MBq), 11.3 nmol/kg (60.4 MBq), or 31.1 nmol/kg (30.8 MBq) of [$^{11}$C]raclopride was obtained on separate days. PET data were acquired for 50 mins with the same protocol as the single PET scan approach. The values of $R_1$, $k_2$, and $BP_{ND}$ were estimated by the SRTM, and $B_{max}$ and $K_d$ were estimated by the conventional graphical analysis.

## Results

### Simulation Study

*Effect of Injected Mass on $BP_{ND}$ Estimates*: In the simulations, the value of $BP_{ND}$, estimated by the MI-SRTM, decreased as injected molar amount of raclopride increased, that is, concentration of bound raclopride became larger. The relationship between $BP_{ND}$ and $B^{ref}$ had a good linear correlation to some extent; however, it did not remain linear for large $B^{ref}$ (Figure 2A). The regression line where $B^{ref} < 20$ pmol/mL was $BP_{ND} = -0.091B^{ref} + 2.4$, $R^2 = 0.997$ for the first injection. In the relationship between $BP_{ND}$ and $B^{ref}$, $BP_{ND}$ values of the third injection were higher than those of the first injection when $B^{ref}$ was lower than 20 pmol/mL. The ratio $B^{ref}/F^{ref}$ was almost the same as the $BP_{ND}$ estimated by MI-SRTM, though it was a little smaller when $B^{ref}$ was lower than 5 pmol/mL (Figure 2B).

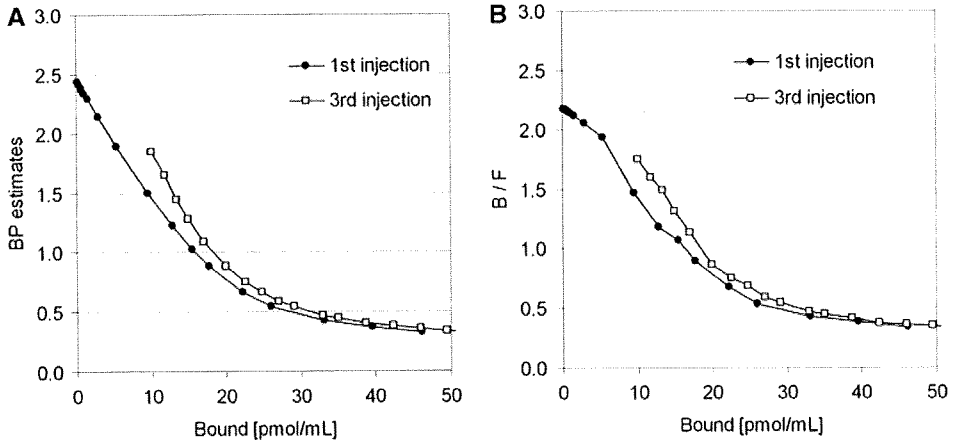


**Figure 2** Relationship between specifically bound concentration and $BP_{ND}$ (**A**) or $B^{ref}/F^{ref}$ (**B**) estimates for the first and third injection in the simulations.

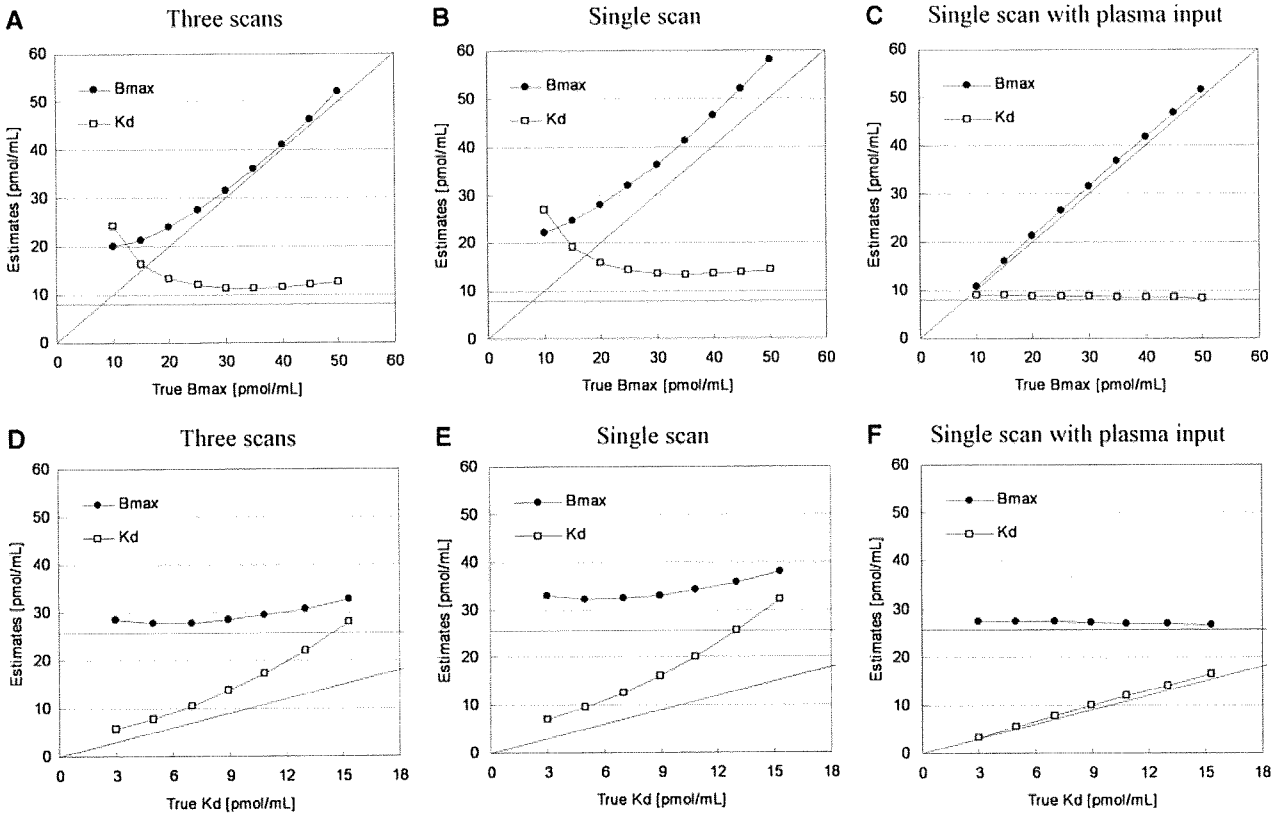


**Figure 3** Relationships between estimates and true values of $B_{max}$ and $K_d$ for simulated TACs with various $B_{max}$ and fixed $K_d$ (**A–C**) and with various $K_d$ and fixed $B_{max}$ (**D–F**) by the three PET scan approach (**A**, **D**), multiple-injection single PET scan approach (**B**, **E**), and single PET scan approach with the plasma input function (**C**, **F**).

*Estimation of $B_{max}$ and $K_d$ Values by the Multiple-Injection Graphical Analysis*: The TACs were calculated for a range of possible $B_{max}$ and $K_d$ values, and the relationship between true and estimated $B_{max}$ or $K_d$ values was investigated for conventional three PET scan and the proposed single PET scan approaches. When $B_{max}$ was varied, $B_{max}$ and $K_d$ were overestimated compared with the true values in both three PET scan and single PET scan approaches (Figures 3A and 3B). However, a good correlation was observed between true and estimated $B_{max}$, and there was little variation in estimated $K_d$ when $B_{max}$ was set higher than 20 pmol/mL. Similarly, when $K_d$ was varied, although $K_d$ and $B_{max}$ were overestimated in both approaches, there was a good correlation between true and estimated $K_d$, and estimated $B_{max}$ was constant (Figures 3D and 3E). In both cases, $B_{max}$ and $K_d$ estimates in the single

PET scan approach were higher than those in the three PET scan approach. In the TAC simulated with $B_{max} = 25.7$ and $K_d = 7.0$, estimated $B_{max}$ and $K_d$ were 27.8 and 10.5, respectively, in the three PET scan approach, and 32.3 and 12.6, respectively, in the single PET scan approach. In contrast to these approaches with the reference TAC, the overestimation of $B_{max}$ and $K_d$ was scarcely observed in the MI-GA with the plasma input function (Figures 3C and 3F).

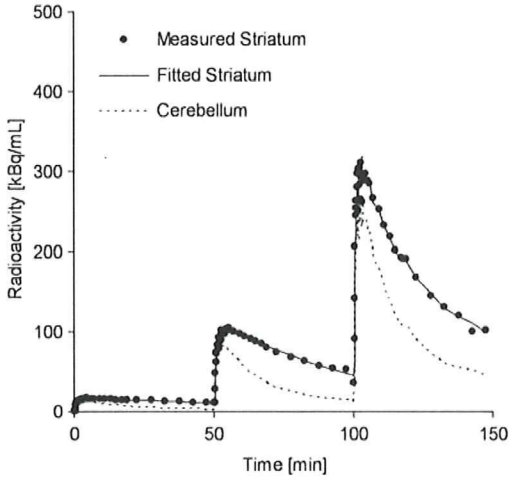


**Figure 4** Measured TACs of the striatum and cerebellum and a fitted curve for the striatum using MI-SRTM in the monkey study by a single scan with sequential three injections of [$^{11}$C]raclopride.

## Monkey Studies

Typical examples of TACs for the striatum and the cerebellum in the multiple-injection study are shown in Figure 4, and the parametric images of $BP_{ND}$ for the first, second, and third injection, and images of $B_{max}$ and $K_d$ for the voxels in which $BP_{ND1}$ was higher than 1.5 are shown in Figure 5. The estimated $BP_{ND}$ decreased as the injected molar amount of [$^{11}$C]raclopride became larger in the second or third injection. Estimated $BP_{ND1}$, $BP_{ND2}$, and $BP_{ND3}$ values were 2.3, 1.4, and 0.74, respectively, in the left striatum, and 2.6, 1.9, and 0.87, respectively, in the right striatum. The reduction in $BP_{ND}$ was also observed in the parametric images.

The plots of MI-GA are shown in Figure 6. Plots of MI-GA for each of three animals were on the line, and $B_{max}$ and $K_d$ could be estimated as summarized in Table 1. Using the single scan approach for the hemiparkinsonian animal, $B_{max}$ was 42.3 pmol/mL and $K_d$ was 15.2 pmol/mL in the affected (right) striatum, and $B_{max}$ was 32.3 pmol/mL and $K_d$ was 13.0 pmol/mL in the contralateral (left) normal striatum. Corresponding estimates for the three scan approach were $B_{max} = 36.4$ and $K_d = 13.3$ pmol/mL in the right striatum and $B_{max} = 29.2$ and $K_d = 11.6$ pmol/mL in the

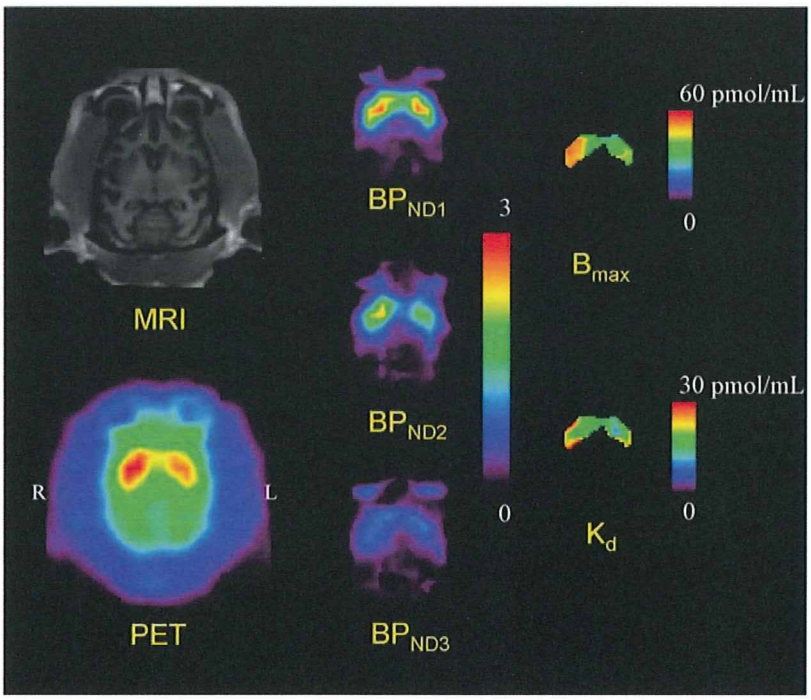


**Figure 5** MRI and PET summation image (left) and parametric images of $BP_{ND}$ for the first, second, and third injection (center) and parametric images of $B_{max}$ and $K_d$ for the voxels in which $BP_{ND1}$ is higher than 1.5 (right) in the unilateral Parkinsonian (monUP) monkey study by a single scan with three sequential injections of [$^{11}$C]raclopride. Although ROI analysis disclosed higher $B_{max}$ values in the MPTP-infused side of the striatum, the parametric image showed more evident increase of $B_{max}$ in the dorsal and posterior parts of the striatum.

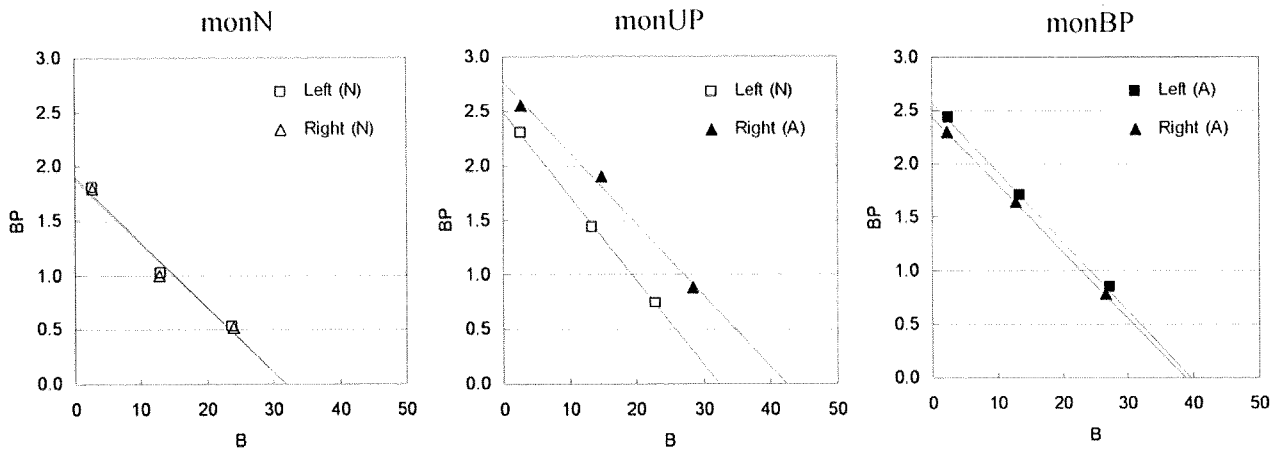


**Figure 6** Single-scan, multiple-injection graphical analysis for normal (N) or affected (A) region of the left or right striatum in three monkeys that were normal (monN), unilateral Parkinsonian (monUP), and bilateral Parkinsonian (monBP).

**Table 1** Estimated $B_{max}$ and $K_d$ values in three monkey studies

| *Scan protocol* | *Subject* | *Region* | *Diagnosis* | $B_{max}$ *(pmol/mL)* | $K_d$ *(pmol/mL)* |
|---|---|---|---|---|---|
| Single scan | monN | L | N | 31.8 | 16.7 |
| | | R | N | 31.7 | 16.9 |
| | monUP | L | N | 32.3 | 13.0 |
| | | R | A | 42.3 | 15.2 |
| | monBP | L | A | 39.6 | 15.4 |
| | | R | A | 38.7 | 15.9 |
| Three scans | monUP | L | N | 29.2 | 11.6 |
| | | R | A | 36.4 | 13.3 |

L, left striatum; R, right striatum; N, normal striatum; A, affected striatum.

left striatum. Both $B_{max}$ and $K_d$ of the single PET scan approach were slightly higher than those of the three PET scan approach. However, importantly, both approaches found that $B_{max}$ in the affected striatum was higher than that in the normal striatum. The bilateral Parkinsonian animal showed $B_{max}$ values of left = 39.6 pmol/mL, right = 38.7 pmol/mL, both of which were higher than those of the striatum of the normal animal or the normal striatum of the unilateral animal, but were very close to the affected striatum of the unilateral animal. The $K_d$ values of the bilateral animal were not so different from other striatums.

## Discussion

### Density and Affinity Determination by Graphical Analysis with the Reference Region

In the graphical analysis for PET receptor studies, the values of $B_{max}$ and $K_d$ were estimated from the relationship between the ratio of bound to free concentrations and bound concentration at the time of transient equilibrium, using the TAC of the reference region (Farde *et al*, 1986). Some groups have used the value estimated from the distribution volume ratio − 1, instead of the $B^{ref}/F^{ref}$ value of the $y$ axis, because the values of $B^{ref}/F^{ref}$ could change considerably with small changes in the time point of the transient equilibrium $T_{eq}$ determined as the maximum $C_b^{ref}$ (Logan *et al*, 1997; Doudet and Holden, 2003; Doudet *et al*, 2003). Distribution volume ratio or $BP_{ND}$ is estimated from the kinetic analysis with TACs of target and reference regions, so it is not affected by the error of estimated $T_{eq}$. On the other hand, the value of $k'_3(t)$ in Equation (2) varies according to the concentration of bound raclopride, and estimates of $BP_{ND}$ are considered to be an averaged value of specific binding over time, which is influenced by the dynamics of the free and bound raclopride. Despite this, in our simulation study of [$^{11}$C]raclopride, there was little difference between $B^{ref}/F^{ref}$ and $BP_{ND}$ estimated by the SRTM, and both had a linear correlation with $B^{ref}$ (Figure 2). However, $B^{ref}/F^{ref}$ became smaller than $BP_{ND}$ and deviated from the linear relationship between $B^{ref}/F^{ref}$ and $B^{ref}$ in the region with low $B^{ref}$ (Figure 2), especially for the TACs with high $B_{max}$. This may be a result of imperfect attainment of the transient equilibrium within the 50 mins scan duration for the TAC with high binding. There was little effect of the error of $B^{ref}$ for the graphical analysis, in which $B^{ref}$ varied widely among three injections, whereas the error of $B^{ref}/F^{ref}$

because of nonachievement of transient equilibrium had much effect on the graphical analysis as compared with $BP_{ND}$. Therefore, we estimated $B_{max}$ and $K_d$ by the graphical analysis with the relationship between $BP_{ND}$ and $B^{ref}$.

In the simulations with various injected masses of [$^{11}$C]raclopride, it was shown that the relationship between $BP_{ND}$ and $B^{ref}$ became linear to some extent. However, $BP_{ND}$ deviated from the linear relationship and approached a nonzero value when $B^{ref}$ became larger (Figure 2). Therefore, in the $B_{max}$ and $K_d$ estimation by the graphical analysis with the reference TAC, points must be plotted within the range of the linear relation. As the relationship between $BP_{ND}$ and $B$ estimated from $C_b$ using the plasma input function, without the reference TAC, remained linear even when $B$ became large and the estimated $BP_{ND}$ approached 0 (data not shown), this apparent saturation seemed to be owing to the reference region. Strictly speaking, the time course of free radioligand $C_f$ is different from that of the reference region $C_r$ (Figure 1) and $C_f$ changes according to the specific binding that was affected by $k_{on}$, $B_{max}$, or administered mass of raclopride as pointed out by Ito *et al* (1998). Therefore, the time of the transient equilibrium estimated using $C_b^{ref}$ was different from that estimated using $C_b$, and $B^{ref}$ was often different as well. In addition, the value of $BP_{ND}$ estimated by SRTM was lower than the $BP_{ND}$ estimated from the two-tissue compartment model with the plasma input function.

This difference between the target and reference TAC affected the $B_{max}$ and $K_d$ estimates as well. In the simulated TACs with various $B_{max}$ or $K_d$ values, the $B_{max}$ and $K_d$ were overestimated compared with the true values even in the conventional three PET scan approach (Figure 3). On the other hand, the overestimation was not observed when $B_{max}$ and $K_d$ were estimated by the graphical analysis using $C_f$ and $C_b$ without the reference TAC (Figure 3), demonstrating that graphical analysis could determine $B_{max}$ and $K_d$ precisely if $C_b$ were obtained correctly. However, the free and bound concentrations in the target region cannot be distinguished from the total concentration measured by PET scanning without arterial blood sampling, and in practical PET data, estimation of rate constants with the plasma input function is unstable and impractical. Therefore, in the usual graphical analysis, the TAC of reference region is used as the free radioligand concentration in the target region (Farde *et al*, 1989). The effect of the reference TAC on $B_{max}$ and $K_d$ estimates depends on the kinetics of the tracer in each region, which depends in turn on the particular tracers and species. In the simulated TACs of monkeys with [$^{11}$C]raclopride, there was a good correlation between true and estimated $K_d$ or $B_{max}$, though estimates were biased. Therefore, we concluded the graphical analysis with reference TAC is practical for [$^{11}$C]raclopride studies, because it can detect the value of $B_{max}$ or $K_d$ in neurological or psychiatric disorders without arterial blood sampling.

### Estimated Density and Affinity by the Multiple-Injection Approach

We applied the multiple-injection approach to the graphical analysis for $B_{max}$ and $K_d$ determination in an effort to shorten the total duration of the scanning protocol, and to obviate the need for several radiosyntheses for each animal. From the relationship between the $BP_{ND}$ estimates and injected mass in the simulation study (Figure 2), the molar amounts of three injections were set as 1.5, 10, and 30 nmol/kg, so that the estimated $BP_{ND}$ would be high, intermediate, and low within the range in which the linear correlation held. The injection interval was set to 50 mins, because it has been reported in monkey studies that 50 mins scan duration could provide reliable $BP_{ND}$ estimates even for TACs with high and low $BP_{ND}$ values (Ikoma *et al*, 2009). In our present studies on monkeys with this protocol, injected masses increased with each successive injection, but amounts of administered radioactivity remained fairly constant, i.e., 57, 60, and 31 MBq. Therefore, the signal to noise ratio of image quality did not change seriously for each injection.

In the usual graphical analysis by nonsequential multiple PET scans, the molar amount of administered [$^{11}$C]raclopride for each scan is adjusted by varying the specific activity of administered [$^{11}$C] raclopride. Several investigators have attempted to perform multiple injections of ligands with PET studies to obtain receptor density and affinity by changing specific activity with a detailed model equation (Delforge *et al*, 1995; Millet *et al*, 1995; Morris *et al*, 1996; Muzic *et al*, 1996; Christian *et al*, 2004; Gallezot *et al*, 2008). Meanwhile, our approach requires only one synthesis of [$^{11}$C]raclopride, which is split to three with different mass of raclopride with same specific activity. By keeping the specific activity throughout scan, we can directly interpret PET counts in pmol/mL unit.

In the simulations of $B_{max}$ and $K_d$ estimation with this single PET scan approach, $B_{max}$ and $K_d$ were overestimated compared with the true values, just as seen in the three PET scan approach. Furthermore, estimates of both parameters were higher than those in the three PET scan approach. In the single PET scan approach, the error because of assumptions of the reference tissue approach could be more severe than for the three PET scan approach, because the residual radioactivities at the times of the second and third injections could propagate to error of $B^{ref}$ or $BP_{ND}$ estimates. This was shown to be the case in the simulation study, in which the relationship between the $BP_{ND}$ and $B^{ref}$ in the third injection was a little different from that in the first injection (Figure 2). Furthermore, our approach assumes that $BP_{ND}$ is promptly altered by the next injection, but this is in fact not exactly the case. We showed the bias of the estimated $BP_{ND}$ related to this assumption (Ikoma *et al*, 2009), and the estimated $B_{max}$ and $K_d$ in this paper consequently could be biased. However, in the

simulations, $B_{max}$ and $K_d$ estimated by the MI-GA changed according to the variation of the true values (Figure 3), demonstrating this approach could be applied to the quantitative evaluation of $B_{max}$ and $K_d$ from a single session of PET scanning.

### Monkey Studies

In the simulations, we demonstrated that the MI-GA could detect density and affinity of dopamine $D_2$ receptors. Furthermore, we demonstrated the validity of the proposed method using actual data from monkeys. As a result, the three $BP_{ND}$ data points calculated from the single PET scan with three sequential injections of different administration masses were almost on a straight line, and estimated values of $B_{max}$ and $K_d$ were very close to those previously obtained *in vitro* ($B_{max} = 25.7$ pmol/g) (Madras *et al*, 1988) or *in vivo* by the conventional method in monkeys ($B_{max} = 22$ pmol/mL, $K_d = 13.5$ nmol/L) (Doudet *et al*, 2003). The estimates by the single PET scan approach were slightly higher than those by the three PET scan approach, and this was consistent with the results from the current simulations.

Although we investigated only three monkeys in this study, the values of $B_{max}$ in the partially denervated striata was higher than in normal striatum, whereas the apparent affinity was unaffected by the MPTP lesions. Likewise Rinne *et al* (1995) reported a 35% increase in the $D_2$ $B_{max}$ in the putamen contralateral to the side of predominant motor symptoms, without any discernible effect on apparent affinity. In our monkey measurements, in the hemilesioned monkey, the $B_{max}$ was elevated by 31% on the denervated side. In the animal with bilateral MPTP lesion, the $B_{max}$ in both striata was higher than in the normal animal, or in the unlesioned side of the hemiparkinsonian animal, despite no significant changes in $K_d$ values: the results were consistent with those of the previous report.

In addition to the results of ROI analysis, which disclosed bulk $D_2$ receptor characteristics in the whole striatum, parametric imaging of $B_{max}$ and $K_d$ (as shown in Figure 5) suggested a potential significance in regional estimation of $D_2$ receptor characteristics. Although ROI analysis disclosed higher $B_{max}$ values in the MPTP-infused side of the striatum, the parametric imaging showed the increase of $B_{max}$ was more evident in the dorsal and posterior parts of the striatum. A similar finding of preferential lesion in dorsal and posterior parts of the striatum has been reported based on neurochemical and pathological assessments of MPTP-lesioned monkeys (Oiwa *et al*, 2003). As the current parametric imaging may have significant artifacts, such as those arising from low signal-to-noise ratio, partial volume effects, small number of points, the situation should be improved through the use of a higher resolution PET scanner.

### Potential Limitations of the Multiple-Injection Graphical Analysis

The multiple-injection approach is able to assess the $B_{max}$ and $K_d$ for receptor studies in a single PET scan with single radiosynthesis, and shortened study period as compared with a conventional approach. This approach might also be applicable to other PET ligands and receptor types, but with several caveats: First, it is necessary to evaluate whether the reference region can be used as the free TAC of the target region. The kinetics of the target and reference regions is affected by the value of each rate constant, i.e., $K_1$, $k_2$, $B_{max}$, and $K_d$, that differ between species and radioligands. The difference between $C_{ref}$ and $C_f$ often causes an error in $B^{ref}$, and the estimated $B_{max}$ and $K_d$ should be interpreted with caution when the reference region has considerably different kinetics. Second, the molar amounts of administered ligand need to be selected such that the resultant $BP_{ND}$ will be within the range in which the linear relationship between $BP_{ND}$ and $B$ holds. In the case of regions with low $BP_{ND}$, and small extent of the necessary linear relationship, it may be difficult to determine $B_{max}$ and $K_d$ reliably. Third, the interval of three injections should be determined so that the free ligand TAC has a transient equilibrium within the scan duration of each injection, especially when the injected mass is small, i.e., $BP_{ND}$ is high. The radioligand [$^{11}$C]raclopride dissociates rapidly from the receptors, allowing equilibration of binding to be established *in vivo* within the time span of PET experiments (Farde *et al*, 1989; Ito *et al*, 1998). However, those ligands with slow kinetics, such as [$^{18}$F]fallypride require a longer scan duration such that the present graphical analysis may not be suitable in all instances. Despite these limitations, by optimizing the administered mass and the time interval between three injections of [$^{11}$C]raclopride, we have shown that the multiple-injection approach can determine $B_{max}$ and $K_d$ values as effectively as an approach using three separate scans, but within a single scan time of 150 mins.

Moreover, the bias of $B_{max}$ and $K_d$ estimated by the single scan approach with two injections was not larger than that by the single scan approach with three injections in the simulations (data not shown), and points of the second and third injections in MI-GA were almost on the same line in the monkey studies (Figure 6). Therefore, there is a possibility of reducing scan time and exposure further using only two injections, though the effect of statistical noise on estimates should be considered.

### Conclusion

We developed the method for estimating $B_{max}$ and $K_d$ values in a single session of PET scanning with multiple injections of [$^{11}$C]raclopride. Our simulations showed that the MI-GA could detect $B_{max}$ and $K_d$ values by using the optimal injection protocol. We

also demonstrated in monkey studies that $B_{max}$ and $K_d$ values estimated by our proposed approach were proper compared with previous monkey studies or our studies by the conventional method. The proposed method made it possible to determine the dopamine $D_2$ receptor density and affinity by a 150 mins PET scan with three injections of [$^{11}$C]raclopride at 50 mins intervals.

## Acknowledgements

We thank Dr Jun Takahashi (Kyoto University) for providing us animals for this study. This research was supported by the Ministry of Education, Culture, Sports, Science and Technology of Japan (MEXT) grant-in-aid for Young Scientists (B) (No. 20790839), grant-in-aid for Scientific Research (C) (No. 09019855) (TH), Kobe Cluster I and II, and the Ministry of Health, Labour, and Welfare of Japan (MHLW) Health Science Research Grant, H17-025 (TH, HI). We are grateful to members of Department of Investigative Radiology, National Cardiovascular Center Research Institute, for their support of PET experiment and for helpful suggestions.

## Conflict of interest

The authors declare no conflict of interest.

## References

Bankiewicz KS, Oldfield EH, Chiueh CC, Doppman JL, Jacobowitz DM, Kopin IJ (1986) Hemiparkinsonism in monkeys after unilateral internal carotid artery infusion of 1-methyl-4-phenyl-1,2,3,6-tetrahydropyridine (MPTP). *Life Sci* 39:7–16

Christian BT, Narayanan T, Shi B, Morris ED, Mantil J, Mukherjee J (2004) Measuring the *in vivo* binding parameters of [$^{18}$F]-fallypride in monkeys using a PET multiple-injection protocol. *J Cereb Blood Flow Metab* 24:309–22

Cross AJ, Crow TJ, Owen F (1981) $^3$H-Flupenthixol binding in post-mortem brains of schizophrenics: evidence for a selective increase in dopamine D2 receptors. *Psychopharmacology (Berl)* 74:122–4

Delforge J, Pappata S, Millet P, Samson Y, Bendriem B, Jobert A, Crouzel C, Syrota A (1995) Quantification of benzodiazepine receptors in human brain using PET, [$^{11}$C]flumazenil, and a single-experiment protocol. *J Cereb Blood Flow Metab* 15:284–300

Doudet DJ, Holden JE (2003) Sequential versus nonsequential measurement of density and affinity of dopamine $D_2$ receptors with [$^{11}$C]raclopride: Effect of methamphetamine. *J Cereb Blood Flow Metab* 23:1489–94

Doudet DJ, Jivan S, Holden JE (2003) *In vivo* measurement of receptor density and affinity: comparison of the routine sequential method with a nonsequential method in studies of dopamine $D_2$ receptors with [$^{11}$C]raclopride. *J Cereb Blood Flow Metab* 23:280–4

Farde L, Ehrin E, Eriksson L, Greitz T, Hall H, Hedström CG, Litton JE, Sedvall G (1985) Substituted benzamides as ligands for visualization of dopamine receptor binding in the human brain by positron emission tomography. *Proc Natl Acad Sci USA* 82:3863–7

Farde L, Eriksson L, Blomquist G, Halldin C (1989) Kinetic analysis of central [$^{11}$C]raclopride binding to $D_2$-dopamine receptors studied by PET — A comparison to equilibrium analysis. *J Cereb Blood Flow Metab* 9: 696–708

Farde L, Hall H, Ehrin E, Sedvall G (1986) Quantitative analysis of $D_2$ dopamine receptor binding in the living human brain by PET. *Science* 231:258–61

Farde L, Wiesel FA, Hall H, Halldin C, Stone-Elander S, Sedvall G (1987) No $D_2$ receptor increase in PET study of schizophrenia. *Arch Gen Psychiatry* 44:671–2

Farde L, Wiesel FA, Stone-Elander S, Halldin C, Nordström AL, Hall H, Sedvall G (1990) $D_2$ dopamine receptors in neuroleptic-naive schizophrenic patients. A positron emission tomography study with [$^{11}$C]raclopride. *Arch Gen Psychiatry* 47:213–9

Gallezot JD, Bottlaender MA, Delforge J, Valette H, Saba W, Dollé F, Coulon CM, Ottaviani MP, Hinnen F, Syrota A, Grégoire MC (2008) Quantification of cerebral nicotinic acetylcholine receptors by PET using 2-[$^{18}$F]fluoro-A-85380 and the multiinjection approach. *J Cereb Blood Flow Metab* 28:172–89

Gunn RN, Lammertsma AA, Hume SP, Cunningham VJ (1997) Parametric imaging of ligand-receptor binding in PET using a simplified reference region model. *Neuroimage* 6:279–87

Guttman M, Seeman P (1985) L-dopa reverses the elevated density of $D_2$ dopamine receptors in Parkinson's diseased striatum. *J Neural Transm* 64:93–103

Hall H, Köhler C, Gawell L, Farde L, Sedvall G (1988) Raclopride, a new selective ligand for the dopamine-$D_2$ receptors. *Prog Neuropsychopharmacol Biol Psychiatry* 12:559–68

Herzog H, Tellmann L, Hocke C, Pietrzyk U, Casey ME, Kuwert T (2004) NEMA NU2-2001 guided performance evaluation of four Siemens ECAT PET scanners. *IEEE Trans Nucl Science* 51:2662–9

Ikoma Y, Watabe H, Hayashi T, Miyake Y, Teramoto N, Minato K, Iida H (2009) Quantitative evaluation of changes in binding potential with a simplified reference tissue model and multiple injections of [$^{11}$C]raclopride. *Neuroimage* 47:1639–48

Ito H, Hietala J, Blomqvist G, Halldin C, Farde L (1998) Comparison of the transient equilibrium and continuous infusion method for quantitative PET analysis of [$^{11}$C]raclopride binding. *J Cereb Blood Flow Metab* 18:941–50

Joyce JN, Lexow N, Bird E, Winokur A (1988) Organization of dopamine $D_1$ and $D_2$ receptors in human striatum: receptor autoradiographic studies in Huntington's disease and schizophrenia. *Synapse* 2:546–57

Köhler C, Hall H, Ogren SO, Gawell L (1985) Specific *in vitro* and *in vivo* binding of $^3$H-raclopride. A potent substituted benzamide drug with high affinity for dopamine D-2 receptors in the rat brain. *Biochem Pharmacol* 34:2251–9

Lammertsma AA, Hume SP (1996) Simplified reference tissue model for PET receptor studies. *Neuroimage* 4:153–8

Logan J, Fowler JS, Volkow ND, Wang GJ, Ding YS, Alexoff DL (1996) Distribution volume ratios without blood sampling from graphical analysis of PET data. *J Cereb Blood Flow Metab* 16:834–40

Logan J, Volkow ND, Fowler JS, Wang GJ, Fischman MW, Foltin RW, Abumard NN, Vitkun S, Gatley SJ, Pappas N, Hitzemann R, Shea CE (1997) Concentration and occupancy of dopamine transporters in cocaine abusers with [$^{11}$C]cocaine and PET. *Synapse* 27:347–56

Madras BK, Fahey MA, Canfield DR, Spealman RD (1988) D1 and D2 dopamine receptors in caudate-putamen of nonhuman primates (*macaca fascicularis*). *J Neurochem* 51:934–43

Millet P, Delforge J, Mauguiere F, Pappata S, Cinotti L, Frouin V, Samson Y, Bendriem B, Syrota A (1995) Parameter and index images of benzodiazepine receptor concentration in the brain. *J Nucl Med* 36:1462–71

Mintun MA, Raichle ME, Kilbourn MR, Wooten GF, Welch MJ (1984) A Quantitative model for the *in vivo* assessment of drug binding sites with positron emission tomography. *Ann Neurol* 15:217–27

Morris ED, Babich JW, Alpert NM, Bonab AA, Livni E, Weise S, Hsu H, Christian BT, Madras BK, Fischman AJ (1996) Quantification of dopamine transporter density in monkeys by dynamic PET imaging of multiple injections of $^{11}$C-CFT. *Synapse* 24:262–72

Muzic RR, Nelson AD, Saidel GM, Miraldi F (1996) Optimal experiment design for PET quantification of receptor concentration. *IEEE Trans Med Imaging* 15:2–12

Oiwa Y, Eberling JL, Nagy D, Pivirotto P, Emborg ME, Bankiewicz KS (2003) Overlesioned hemiparkinsonian non human primate model: correlation between clinical, neurochemical and histochemical changes. *Front Biosci* 8:155–66

Rinne JO, Laihinen A, Ruottinen H, Ruotsalainen U, Någren K, Lehikoinen P, Oikonen V, Rinne UK (1995) Increased density of dopamine $D_2$ receptors in the putamen, but not in the caudate nucleus in early Parkinson's disease: a PET study with [$^{11}$C]raclopride. *J Neurol Sci* 132:156–61

Scatchard G (1949) The attractions of proteins for small molecules and ions. *Ann NY Acad Sci* 51:660–72

Seeman P, Bzowej NH, Guan HC, Bergeron C, Reynolds GP, Bird ED, Riederer P, Jellinger K, Tourtellotte WW (1987) Human brain $D_1$ and $D_2$ dopamine receptors in schizophrenia, Alzheimer's, Parkinson's, and Huntington's diseases. *Neuropsychopharmacology* 1:5–15

Takagi Y, Takahashi J, Saiki H, Morizane A, Hayashi T, Kishi Y, Fukuda H, Okamoto Y, Koyanagi M, Ideguchi M, Hayashi H, Imazato T, Kawasaki H, Suemori H, Omachi S, Iida H, Itoh N, Nakatsuji N, Sasai Y, Hashimoto N (2005) Dopaminergic neurons generated from monkey embryonic stem cells function in a Parkinson primate model. *J Clin Invest* 115:102–9

Watabe H, Ohta Y, Teramoto N, Miyake Y, Kurokawa M, Yamamoto A, Ose Y, Hayashi T, Iida H (2006) A novel reference tissue approach for multiple injections of [C-11]Raclopride. *Neuroimage* 31:T73

Wong DF, Wagner Jr HN, Tune LE, Dannals RF, Pearlson GD, Links JM, Tamminga CA, Broussolle EP, Ravert HT, Wilson AA, Toung JK, Malat J, Williams JA, O'Tuama LA, Snyder SH, Kuhar MJ, Gjedde A (1986) Positron emission tomography reveals elevated $D_2$ dopamine receptors in drug-naive schizophrenics. *Science* 234:1558–63

## Appendix

The multiple-injection two-tissue four-parameter compartment model is based on the following differential equations:

$$\frac{dC_f}{dt} = K_1 C_p(t) - (k_2 + k_3) C_f(t) + k_4 C_b(t) \qquad \text{(A1)}$$

$$\frac{dC_b}{dt} = k_3 C_f(t) - k_4 C_b(t) \qquad \text{(A2)}$$

where $C_p$ is the radioactivity concentration of metabolite-corrected plasma, $C_f$ and $C_b$ are the concentrations of radioactivity for free and specifically bound ligand in tissue, respectively.

Equations (A1) and (A2) are solved with the radioactivity concentration of $C_f$ and $C_b$ at the time of injection, that is $C_f(0)$ and $C_b(0)$, then $C_f(t)$, $C_b(t)$ and total radioactivity concentration in tissue $C_t(t)$ are expressed as following equations:

$$\begin{aligned} C_f(t) = {} & \frac{K_1}{\alpha_2 - \alpha_1}\{(k_4 - \alpha_1)e^{-\alpha_1 t} - (k_4 - \alpha_2)e^{-\alpha_2 t}\} \otimes C_p(t) \\ & + \frac{1}{\alpha_2 - \alpha_1}\{(k_4 - \alpha_1)C_f(0) + k_4 C_b(0)\}e^{-\alpha_1 t} \\ & - \frac{1}{\alpha_2 - \alpha_1}\{(k_4 - \alpha_2)C_f(0) + k_4 C_b(0)\}e^{-\alpha_2 t} \end{aligned} \qquad \text{(A3)}$$

$$\begin{aligned} C_b(t) = {} & \frac{K_1 k_3}{\alpha_2 - \alpha_1}(e^{-\alpha_1 t} - e^{-\alpha_2 t}) \\ & \otimes C_p(t) + \frac{k_3}{\alpha_2 - \alpha_1}\left(C_f(0) + \frac{k_4}{k_4 - \alpha_1} C_b(0)\right)e^{-\alpha_1 t} \\ & - \frac{k_3}{\alpha_2 - \alpha_1}\left(C_f(0) + \frac{k_4}{k_4 - \alpha_2} C_b(0)\right)e^{-\alpha_2 t} \\ & + \left(\frac{k_3 k_4}{(k_4 - \alpha_1)(k_4 - \alpha_2)} + 1\right) C_b(0) e^{-k_4 t} \end{aligned} \qquad \text{(A4)}$$

$$\begin{aligned} C_t(t) = {} & \frac{K_1}{\alpha_2 - \alpha_1}\{(k_3 + k_4 - \alpha_1)e^{-\alpha_1 t} - (k_3 + k_4 - \alpha_2)e^{-\alpha_2 t}\} \\ & \otimes C_p(t) + \frac{k_3 + k_4 - \alpha_1}{\alpha_2 - \alpha_1}\left(C_f(0) + \frac{k_4}{k_4 - \alpha_1} C_b(0)\right)e^{-\alpha_1 t} \\ & - \frac{k_3 + k_4 - \alpha_2}{\alpha_2 - \alpha_1}\left(C_f(0) + \frac{k_4}{k_4 - \alpha_2} C_b(0)\right)e^{-\alpha_2 t} \\ & + \left(\frac{k_3 k_4}{(k_4 - \alpha_1)(k_4 - \alpha_2)} + 1\right) C_b(0) e^{-k_4 t} \\ \alpha_{1,2} = {} & \frac{(k_2 + k_3 + k_4) \mp \sqrt{(k_2 + k_3 + k_4)^2 - 4k_2 k_4}}{2} \end{aligned} \qquad \text{(A5)}$$

diagnostic performance of coronary CTA for detection of significant disease was compared to conventional coronary angiography (CCA) in 52 patients.
**Results:** The mean arterial attenuation was 321±20 HU. Enhancement differences across arterial sites were not significant (p> 0.5; one-way analysis of variance using post-hoc Bonferroni correction). The mean arterio-venous attenuation difference (209 HU) was significant across all anatomic regions (p < 0.001). Atherosclerosis was observed in 238/995 (24%) coronary and 368/2441 (15%) systemic arterial segments. Significant stenosis and occlusions were present in 214 (21%) and 24 (2.5%) coronary segments, respectively, whereas asymptomatic > 50% stenosis was present in 49 extracoronary segments. Treatment strategy was modified in 19 (24%) patients based on WBCTA results. The sensitivity, specificity, and positive and negative predictive values of coronary CTA were 78, 94, 78 and 94%, respectively.
**Conclusion:** Comprehensive cardiovascular imaging can be performed effectively with WB-CTA. Pre-clinical assessment of total cardiovascular burden can have significant outcome on secondary prevention.

## C-819

**Intracranial arterial fenestration: Frequency on CT angiography in patients with and without aneurysm**

A. Hasanefendioglu Bayrak, H. Öztürkmen Akay, C. Akgül Özmen, S. Sentürk, H. Nazaroglu; *Diyarbakır/TR (aylin_has@yahoo.com)*

**Purpose:** The frequency of intracranial fenestration is reported as lower than 1% in previous studies with conventional angiography. Our goal is to determine the frequency of fenestration on CT angiography in patients with and without cerebral aneurysm, and to search co-existing vascular variants with fenestration.
**Methods and Materials:** Between September 2007 and May 2008, CT angiographies of 145 patients, performed by 64-sliced CT, were retrospectively reviewed for aneurysm, fenestration and other vascular variants. Nine of the 145 examinations were excluded from the study due to improper technique. The remaining patients (age range 4-96 years, mean 49.3±18) were divided into two groups: 44 patients with aneurysm (group A), and 92 patients without aneurysm (group B). Both groups were investigated for frequency of fenestration and co-existing vascular variants.
**Results:** Fenestration was determined in 6 patients (13.6%) in group A, and in 7 patients (7.6%) in group B. However, the difference was not statistically significant (p: 0.355). We observed that localization of fenestration was close to aneurysm in two patients, whereas other fenestrations were all remote from the aneurysms. In patients with fenestration, we did not observe any variations in anterior circulation; however, 3 patients had variations in posterior circulation. Interestingly, the fenestrations of these patients were also in posterior circulation.
**Conclusion:** There is no significant relationship with presence of aneurysm and fenestration. The frequency of fenestration observed in this study is higher than previous studies with conventional angiography, probably due to scope of CT angiography such as thin sliced images and post-processing procedures.

## C-820

**Increased subclinical atherosclerosis in patients with metabolic syndrome: Whole-body CT angiography for quantitative arterial involvement - results from a comparative study with a control population**

A. Napoli, D. Geiger, P. Di Paolo, F. Zaccagna, C. Catalano, R. Passariello; *Rome/IT (alessandro.napoli@uniroma1.it)*

**Purpose:** Investigate the association between metabolic syndrome (MetS) and subclinical atherosclerosis determined by 64-row whole body CT angiography (WB-CTA) in comparison with a matched control group (non-MetS).
**Methods and Materials:** 64-row WB-CTA was performed in 50 consecutive patients with known MetS and 50 consecutive non-MetS subjects with high cardiovascular risk indices (CI) for total atherosclerotic burden. A 64x0.6 mm detector configuration with an adapted contrast [400 mgI/mL] injection protocol was used. Coronary and extracoronary arteries were divided into 15 and 32 segments, respectively. CI was defined as the cumulative arterial involvement severity at all locations in each patient. CI, MetS, and non-MetS were evaluated with multivariable regression and area under receiver-operator characteristic curve (AUC-ROC) analyses.
**Results:** 612 coronary and 1566 extracoronary arterial segments were evaluated quantitatively in the MetS group compared with 548 coronary and 1595 extracoronary segments in the non-MetS control. Subclinical atherosclerotic lesions were observed in 121 (20%) coronary and 208 (13%) extracoronary segments in MetS patients while 59 (11%) and 156 (10%) asymptomatic atherosclerotic lesions were noted in coronary and extracoronary vessels, respectively, in non-MetS patients. CI values were higher among MetS patients. CI increased with the number of risk components present (MetS: r=0.991, p < 0.001; non-MetS: r=0.896, p=0.059). MetS better predicted the cardiovascular index ≥75$^{th}$ percentile than non-MetS (AUC = 0.539 [95%CI: 0.513 to 0.601).
**Conclusion:** 64-row WB-CTA is an emerging non-invasive modality for imaging atherosclerosis in coronary and extracoronary arteries. Subclinical detection of total atherosclerotic burden in patients with high cardiovascular risk has potential for preventive therapy.

## C-821

**Growth characteristics of the aortic aneurysms: Three-dimensional CT assessment**

H. Naito[1], Y. Hori[1], T. Watabe[1], T. Nakazawa[1], A. Kohno[1], S. Kanzaki[1], T. Fukuda[1], M. Higashi[1], N. Yamada[1], S. Yoneyama[2]; [1]*Osaka/JP*, [2]*Tokyo/JP (hnaito@hsp.ncvc.go.jp)*

**Purpose:** To evaluate directional heterogeneity of wall extension in the growth of aneurysms using volume data of the aorta obtained by follow-up MDCT.
**Methods and Materials:** Eleven male patients aged 46 to 83 years, with atherosclerotic aortic aneurysms (10 thoracic/8 abdominal, middle-sized, fusiform) received 38 contrast-enhanced MDCT including follow-up examinations. From CT images, 3D-reconstruction of whole aorta was performed in workstation with intelligent software (Amira™, MERCURY Computer systems, USA). Then, mean circumferential length (CL) and longitudinal height (H) of aneurysmal aortic wall were calculated from computer-measured length, external volume and surface area of the aneurysm. Extension rates (%/year) of CL and H calculated in each of 79 follow-up CT pairs were compared with maximum diameter (D-max), volume of wall calcification, and ruggedness of the aneurysm assessed by color display of curvature radius.
**Results:** Extension rates of H were greater significantly than CL in aneurysms of under 5 cm in D-max (1.08% vs. 1.01%, p < 0.0001), whereas in aneurysms with D-max > 5 cm no statistical difference between both extension rates and linear increase of CL rates along with D-max increase (R=0.91) were observed. Markedly rugged aneurysms showed significantly greater extension rates of CL (p < 0.0001) and no different H rates compared to those values of smooth-surfaced aneurysms. Calcification volume had no correlation with extension of aneurysmal aortic wall.
**Conclusion:** This study suggested the growth and remodeling processes of aortic aneurysms, initial longitudinal extension of the wall followed by circumferential extension, accelerated and exaggerated with widening and focal protrusion of the aneurysm.

## C-822

**Evaluation with CT-angiography of aortic and supraaortic emergencies after blunt trauma**

E. Zabía Galíndez, M. Pérez Núñez, S. Borruel Nacenta, M. Castaño Reyero, A. Robles Alonso, R. Carrera Terrón; *Madrid/ES (elenazabia@hotmail.com)*

**Learning Objectives:** To illustrate the imaging spectrum of aortic and supraaortic vascular lesions after blunt trauma, with particular emphasis on thoracic inlet and neck vascular injuries. To review the proper CT-angiography protocol and postprocessing techniques in the evaluation of suspected vascular lesions, especially of the supraaortic vessels.
**Background:** Imaging assessment of vascular injuries has traditionally relied on catheter angiography. Vascular lesions are a clinical emergency and a high suspicion index is required for their accurate and rapid diagnosis. Recent developments in MDCT and postprocessing techniques are making CT-angiography a fast and excellent imaging modality for patients with blunt trauma and for initial supraaortic vessels evaluation.
**Imaging Findings:** Imaging findings are presented based on our Level I Trauma center experience. We review the radiologic appearance of the main aortic and supraaortic vascular injuries after blunt trauma, excluding arteriovenous fistulas because of their low frequency with this injury mechanism. Vessel response to injury is limited to either partial wall damage or total wall disruption. Specific signs of arterial injury include intramural hematoma, arterial narrowing, occlusion, contained (pseudoaneurysm) or free (active bleeding with or without arterial transection) contrast extravasation, intimal flap and dissection.
**Conclusion:** CT-angiography is noninvasive and allows prompt and accurate diagnosis of traumatic vascular and extravascular lesions. Conventional angiography remains the gold standard to confirm vascular injuries but is invasive, time-consuming and not optimal as a screening technique. With improved multiplanar and three-dimensional postprocessing techniques, MDCT images can be more accurately reproduced, similar to the familiar angiographic display.

Eur Radiol (2009) 19: 1019–1024
DOI 10.1007/s00330-008-1213-5

NEURO

Yoshiyuki Watanabe
Kensuke Uotani
Tetsuro Nakazawa
Masahiro Higashi
Naoaki Yamada
Yoshiro Hori
Suzu Kanzaki
Tetsuya Fukuda
Toshihide Itoh
Hiroaki Naito

# Dual-energy direct bone removal CT angiography for evaluation of intracranial aneurysm or stenosis: comparison with conventional digital subtraction angiography

Received: 6 June 2008
Revised: 11 August 2008
Accepted: 22 September 2008
Published online: 11 November 2008


Y. Watanabe · K. Uotani · T. Nakazawa · M. Higashi · N. Yamada · Y. Hori · S. Kanzaki · T. Fukuda · H. Naito
Department of Radiology, National Cardiovascular Center, Osaka, Japan

Y. Watanabe (✉)
Department of Radiology, St. Luke's International Hospital, 9-1 Akashicho, Chuo-ku, Tokyo, 104-8565, Japan
e-mail: yowatana@luke.or.jp
Tel.: +81-6-68335012
Fax: +81-6-68727486

T. Itoh
Siemens Asahi Medical Technologies, Tokyo, Japan

**Abstract** Dual energy CT can be applied to bone elimination for cerebral CT angiography (CTA). The aim of this study was to compare the results of dual energy direct bone removal CTA (DE-BR-CTA). To those of DSA. Twelve patients with intracranial aneurysms and/or ICA stenosis were performed on a dual-source CT in dual energy mode. A post-processing software selectively remove bone structures using the two energy data sets. 3D-images with and without bone removal were reviewed and compared to DSA. Dual energy bone removal was successful in all patients. For 10 patients, bone removal was good and CTA MIP images could be used for vessel evaluation. For 2 patients, bone removal was moderate with some bone remnants but this did not disturb the 3D visualization. Three aneurysms adjacent to the skull base were only partially visible in conventional CTA but were fully visible in DE-BR-CTA. In 5 patients with ICA stenosis, DE-BR-CTA revealed the stenotic lesions on the MIP images. The correlation between DSA and DE-BR-CTA was good ($R^2$=0.822), but DE-BR-CTA lead to an overestimation of stenosis. DE-BR-CTA is able to eliminate bone structure using only a single CT data acquisition and is useful to evaluate intracranial aneurysms and stenosis.

**Keyword** Cerebral CTA · Dual-energy CT · Dual-source CT · Bone elimination · Brain

## Introduction

Cerebral computed tomography angiography (CTA) has become a powerful, noninvasive diagnostic tool for evaluating cerebrovascular disease [1–3]. However, single-source CTA still has drawbacks compared to digital subtraction angiography (DSA), in particular for the evaluation of arteries with calcified plaque or vessels located next to the skull bone, as these vasculatures cannot be unambiguously distinguished from surrounding bony or calcified structures. This problem can be solved by applying subtracting CTA to a noncontrast and a contrast CT data set to eliminate bones [4–8]. Dual-source, dual-energy CT has the potential to distinguish iodine from bone or calcifications using the attenuation difference between the two energies [9].

Here, we evaluated the performance of dual-energy direct bone removal CTA (DE-BR-CTA) for diagnosing

brain aneurysms, internal carotid artery (ICA) stenosis, or both. We also compared the DE-BR-CTA findings with those of DSA.

## Materials and methods

### Subjects

This study was performed after obtaining approval of the local institutional review board. Written informed consent was obtained from all patients. We prospectively selected 12 patients (7 male, 5 female; 36–78 years, mean 64 years) who underwent both DE-BR-CTA and DSA within 30 days of each other. Nine patients were suspected of intracranial unruptured aneurysms with MR angiography. Five patients were suspected of ICA stenosis. Of these five, three patients had a stroke and in two patients the asymptomatic stenosis was found during the evaluation for aneurysm.

### CTA protocol

CTA was performed using a dual-source CT system (SOMATOM Definition, Siemens, Germany). CT parameters in the dual-energy mode were 140 and 80 kV tube voltage, 80 and 360 effective mAs, respectively, 0.5-s rotation time, 64×0.6-mm collimation with z-flying focal spot, and a pitch of 0.6. The 140 and 80 kV images (dual-energy images) were reconstructed separately in sections that were 0.75 mm wide at 0.5 mm increments using a D30 kernel for a field of view of 180 mm. Contrast material (350 mg I/ml) was injected for 20 s via the antecubital vein, followed by a 25 ml saline flush. Injection rate and dose depended on the patient's weight: 3.0 ml/s, 60 cc for patients weighing less than 60 kg; 3.5 ml/s, 70 cc for patients weighing less than 70 kg; and 4 ml/s, 80 cc for those over 70 kg. The delay time of the CT data acquisition after the injection was determined using a bolus tracking software at the basilar artery or ICA.

DSA was performed using a biplane DSA unit with rotational 3D DSA (INTEGRIS BV3000, Philips Healthcare, Best, Netherland).

### Image processing and analysis

The dual-energy images were transferred to a workstation (Multi Modality Workplace; Siemens Medical Solutions, Germany), and the prototype of a commercial software (Syngo 2008G) was used to create a DE-BR-CTA from which the bone voxels had been removed ("head bone removal" application). The combined images of both energy data were reconstructed and used for diagnostic reading (conventional CTA).

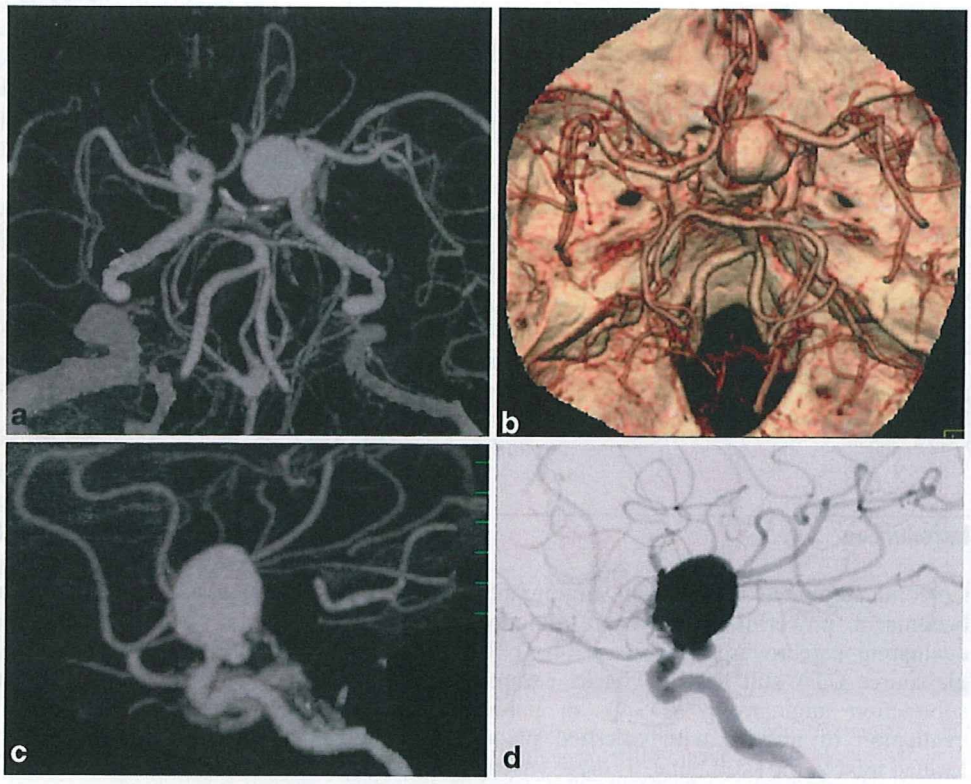


**Fig. 1** Right ICA large aneurysm of a 75-year-old female patient. MIP images of DE-BR-CTA (**a**, **c**) delineate the general shape and configuration of aneurysm as well as DSA (**d**). VR image of conventional CTA (**b**) did not show the caudal side of aneurysm with bone

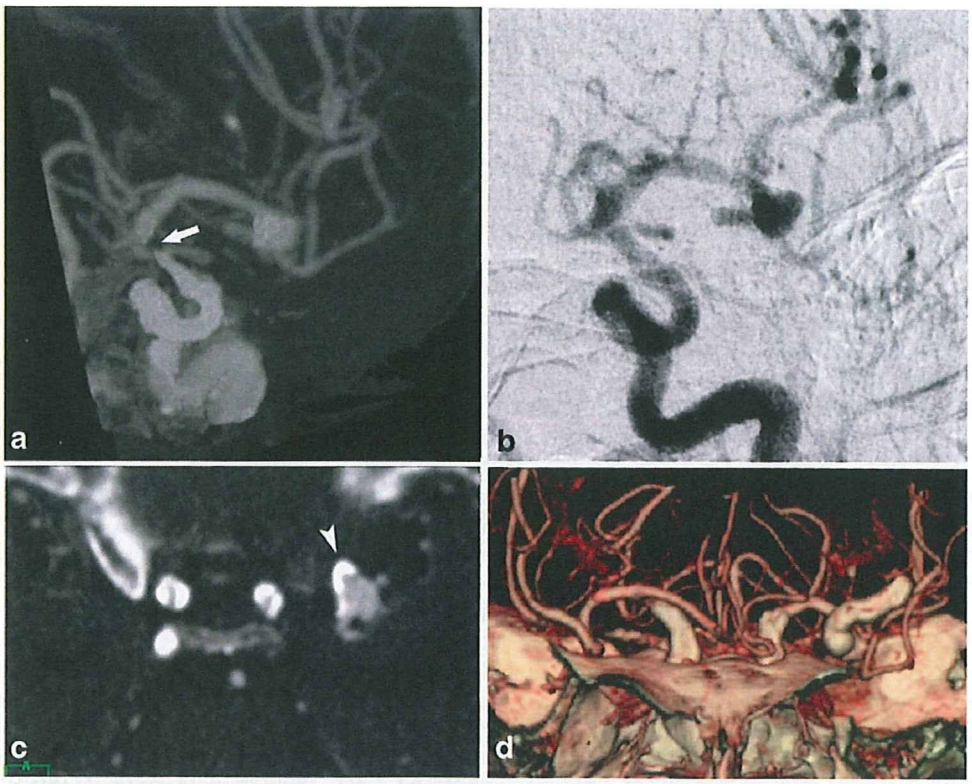


**Fig. 2** Left MCA calcified aneurysm and bilateral ICA stenosis with hard plaque in a 77-year-old female patient. MIP image of DE-BR-CTA (**a**) removed the calcifications of ICA and aneurysm and revealed the same aneurysm shape as with DSA (**b**). However, the DE-BR-CTA (**a**) shows a short defect at the severe stenotic site at ICA terminal (*arrow*). CTA source images (**c**) show dense calcifications around the whole circumference of the ICA and anterior wall of the left MCA aneurysm (*arrowheads*). VR image of conventional CTA (**d**) showed the dense calcification at bilateral ICA and aneurysms, but failed to reveal details

Two neuroradiologists blinded to all clinical information independently reviewed the DE-BR-CTA in maximum-intensity projection (MIP) and the conventional CTA in volume-rendering (VR) technique on a 3D workstation. Disagreements regarding final conclusions were resolved by consensus.

The quality of the dual-energy bone removal was rated according to a four-point scale. "Excellent" was defined as clearly visible vasculature and no bone remnants, "good" as discernable vasculature and containing only tiny bone remnants, "moderate" as containing larger bone remnants that did not however disturb the vessel visualization, and

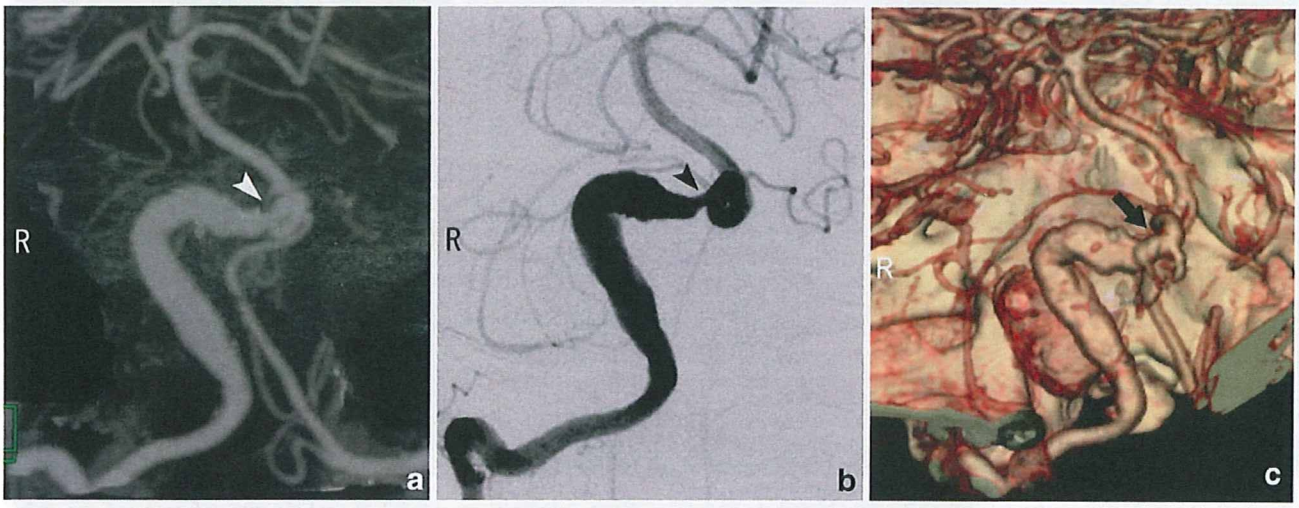


**Fig. 3** Right vertebral artery fusiform aneurysm with calcification in a 55-year-old male patient. MIP image of DE-BR-CTA (**a**) removed the calcification of aneurysm and revealed the distal-end stenosis (*arrowhead*) of the aneurysm as with DSA (**b**). VR image of conventional CTA (**c**) showed the calcification (*arrow*), but the stenosis is hard to see

"poor" as including large bone remnants or artifacts covering parts of the vessels.

Further, the visibility of the ophthalmic artery in DE-BR-CTA was rated according to a four-point scale. "Excellent" was defined as the ophthalmic artery being visible from the origin to the intra-orbital portion, "good" as one artery being visible and the other with only the origin or other short segments being detected, "poor" as the long segment of the ophthalmic artery being detected, and "not visible" as the ophthalmic artery not being discernable at all.

For the evaluation of aneurysm, conventional CTA and DE-BR-CTA were compared for the detection and delineation of aneurysms and compared to the DSA results.

For the evaluation of ICA stenosis, the DE-BR-CTA and DSA were compared and the degree of stenosis was calculated using the Warfarin-Aspirin Symptomatic Intracranial Disease Study method [10], which is the ratio of the diameter of the maximum stenotic site to the diameter of the proximal normal ICA.

Kappa statistics were used to assess interobserver reliability. Kappa values above 0 were considered to indicate positive agreement: less than 0.4, positive but poor agreement; 0.41–0.75, good agreement; and more than 0.75, excellent agreement.

## Results

Dual-energy bone removal was successful in all patients and the post-processing of DE-BR-CTA took an average of 53 s, excluding data transfer and saving time. The quality of dual-energy bone removal was rated "excellent" for two of the patients, "good" for eight patients, and "moderate" for two patients.

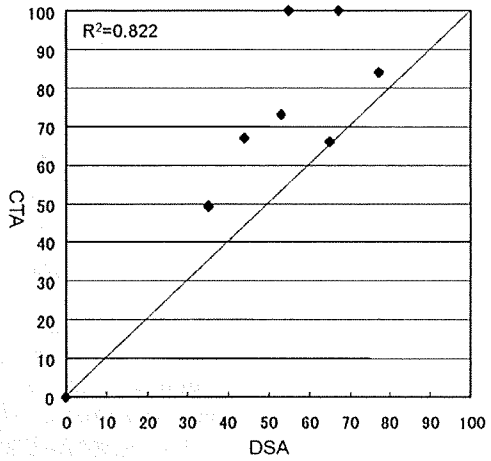


**Fig. 5** Scatterplots illustrate percentages of carotid artery stenosis at DE-BR-CTA versus DSA. Good correlation was noted between the two methods ($R^2$=0.822), but the stenosis diagnosed by CTA was higher than that by DSA for most cases

Of the 24 ophthalmic arteries, the visibility of 7 was rated "excellent," 14 were rated "good," 1 was rated "poor," and 2 arteries were rated "not visible." The two ophthalmic arteries that were not visible in DE-BR-CTA were found by DSA to be occluded. Interobserver reliability between two readers was good for quality of bone removal (k=0.60) and visibility of ophthalmic arteries (k=0.65).

Aneurysms were located in the vertebral artery (two patients), basilar artery (one patient), ICA (two patients),

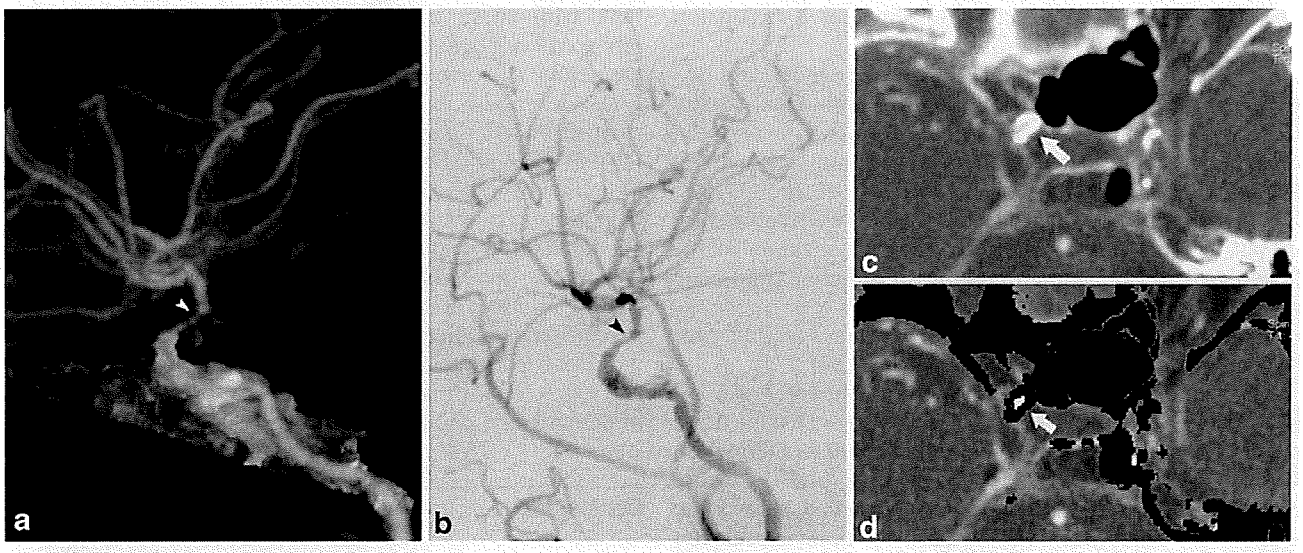


**Fig. 4** Right ICA severe stenosis of a 67-year-old female patient. C2 portion of ICA had severe stenosis (*arrowhead*) demonstrated by DE-BR-CTA (**a**) and DSA (**b**). The ophthalmic artery is not visualized by DE-BR-CTA or by DSA. CTA source images (**c**) show dense calcifications around the whole circumference of the right ICA, and these calcifications were removed after DE bone-removal post-processing (**d**)

middle cerebral artery (MCA; three patients) and anterior communicating artery (ACOM; one patient).

Three aneurysms (two ICA and one MCA) adjacent to the skull base were only partially visible in conventional CTA but were fully visible in DE-BR-CTA (Fig. 1). For three aneurysms with calcifications [two MCA and one vertebral artery (VA)], the calcifications were removed by the head bone removal applications, and the intraluminal shape of the aneurysms was visualized precisely with results confirmed by DSA (Figs. 2, 3).

In five patients with ICA stenosis by calcification at the intercavernous or paraclinoid portion, the eight stenotic lesions were not visible in conventional CTA. However, after bone removal post-processing with dual energy, all stenotic lesions became clearly visible on the MIP images (Figs. 2, 4). The agreement of percent stenosis for the two methods is represented in the scatterplots shown in Fig. 5. The correlation between DSA and CTA was good ($R^2$= 0.822), and the majority of discordant points were above the line of correlation, indicating an overestimation of stenosis found on DE-BR-CTA compared to DSA.

## Discussion

Our study shows that bone removal brain CTA using dual-energy data was useful to evaluate aneurysms and ICA stenosis with a short calculating time, and the results with DE-BR-CTA were comparable to those with DSA.

Dual-energy CT was developed during the late 1970s for tissue characterization using single-source, single-slice CT [11, 12] and mainly applied for bone densitometries [13, 14]. However, the limitation of CT hardware and software technology hampered expansion to further clinical applications [15].

Dual-source CT with dual-energy mode can acquire two different energy data into a single acquisition. Dual-energy CT imaging makes it possible to differentiate between certain materials, since X-ray absorption is material specific and dependent on the energy of the X-rays. Dual-energy CT for tissue characterization was reported for urinary stone differentiation [16–18], visualization of the knee ligament [19], and differentiation of iodine from bone and calcification [9].

Multi-slice CTA has a high sensitivity and specificity for the detection of intracranial aneurysm [1, 20].

Subtraction methods for bone removal in cerebral CTA have been reported for the evaluation of skull base aneurysm or extracranial ICA, such as simple subtraction from enhanced data to noncontrast data [4, 21]. More recently, selective bone removal or "matched mask bone elimination" have been widely used for bone-subtraction CTA where the bone mask image as well as the 3D registration to the enhanced CT acquisition were determined by a low-dose unenhanced CT acquisition [6–8].

In our study, DE-BR-CTA removed the bone structures very well, and the three aneurysms adjacent to the skull base were fully visible from all directions, in contrast to the partial view in conventional CTA.

Calcification of the aneurysmal wall makes surgical clipping difficult, so this information was important for deciding treatment strategies [22]. Conventional CTA images revealed calcifications but neither VR nor MIP images allowed a precise evaluation of the intraluminal aneurysmal shape. By comparison, the geometry of intraluminal aneurysms was clearly visible on DSA, yet calcifications could not be displayed. We found that calcifications of three aneurysms were removed by dual-energy bone removal, therefore the wall and luminal information of the aneurysms could be analyzed with both DE-BR-CTA and conventional CTA.

The advantage of the dual-energy bone removal method compared to CT digital subtraction methods is that it avoids the additional preliminary unenhanced CT acquisition. Single data acquisition reduces the radiation dose to the patient and also shows no misregistration artifacts. Subtraction methods use position adjustment, but if a patient moves between the two consecutive acquisitions, it becomes difficult to achieve a perfect match between the two images.

For the evaluation of intracranial stenosis and occlusion, DSA has been considered the reference standard [10]. The correlation between degree of intracranial stenosis based on CTA and DSA was excellent [23], and CTA has a higher sensitivity and positive predictive value than MRA [24]. Evaluation of ICA stenosis at the petrosal portion of carotid siphon or in cases of calcified plaque has not been reported previously, because CTA did not allow 3D visualization of ICA with these conditions. In contrast, DE-BR-CTA removed bone and calcifications and was able to measure the degree of stenosis.

As described above, we quantitatively evaluated ICA stenosis on MIP image. The correlation coefficient between DE-BR-CTA and DSA results was good, but stenosis tends to be overestimated in DE-BR-CTA compared to DSA. In our study, two severe stenotic arteries were misclassified as occluded (100% stenosis) with DE-BR-CTA. The main reason for this overestimation is blooming effects from calcifications. The poor enhancement of an artery with severe stenosis compared to a nonstenotic artery also makes it difficult to draw a clear demarcation between calcification and iodine. This problem might be resolved by optimization of demarcation parameters and reconstruction kernel.

## Conclusion

Dual-energy bone removal using dual-source CT is able to eliminate bone and calcification from CTA images using only a single contrast-enhanced scan. DE-BR-CTA is a useful tool to evaluate intracranial aneurysms and stenosis.

## References


1. Agid R, Lee SK, Willinsky RA et al (2006) Acute subarachnoid hemorrhage: using 64-slice multidetector CT angiography to "triage" patients' treatment. Neuroradiology 48(11):787–794
2. Hashimoto H, Iida J, Hironaka Y et al (2000) Use of spiral computerized tomography angiography in patients with subarachnoid hemorrhage in whom subtraction angiography did not reveal cerebral aneurysms. J Neurosurg 92(2):278–283
3. Hirai T, Korogi Y, Ono K et al (2001) Preoperative evaluation of intracranial aneurysms: usefulness of intraarterial 3D CT angiography and conventional angiography with a combined unit-initial experience. Radiology 220(2):499–505
4. Jayakrishnan VK, White PM, Aitken D et al (2003) Subtraction helical CT angiography of intra- and extracranial vessels: technical considerations and preliminary experience. AJNR Am J Neuroradiol 24(3):451–455
5. Lell M, Anders K, Klotz E et al (2006) Clinical evaluation of bone-subtraction CT angiography (BSCTA) in head and neck imaging. Eur Radiol 16(4):889–897
6. Sakamoto S, Kiura Y, Shibukawa M et al (2006) Subtracted 3D CT angiography for evaluation of internal carotid artery aneurysms: comparison with conventional digital subtraction angiography. AJNR Am J Neuroradiol 27 (6):1332–1337
7. Tomandl BF, Hammen T, Klotz E et al (2006) Bone-subtraction CT angiography for the evaluation of intracranial aneurysms. AJNR Am J Neuroradiol 27 (1):55–59
8. Venema HW, Hulsmans FJ, den Heeten GJ (2001) CT angiography of the circle of Willis and intracranial internal carotid arteries: maximum intensity projection with matched mask bone elimination-feasibility study. Radiology 218(3):893–898
9. Johnson TR, Krauss B, Sedlmair M et al (2007) Material differentiation by dual energy CT: initial experience. Eur Radiol 17(6):1510–1517
10. Samuels OB, Joseph GJ, Lynn MJ et al (2000) A standardized method for measuring intracranial arterial stenosis. AJNR Am J Neuroradiol 21(4):643–646
11. Chiro GD, Brooks RA, Kessler RM et al (1979) Tissue signatures with dual-energy computed tomography. Radiology 131(2):521–523
12. Millner MR, McDavid WD, Waggener RG et al (1979) Extraction of information from CT scans at different energies. Med Phys 6(1):70–71
13. Genant HK, Boyd D (1977) Quantitative bone mineral analysis using dual energy computed tomography. Invest Radiol 12(6):545–551
14. Laval-Jeantet AM, Cann CE, Roger B et al (1984) A postprocessing dual energy technique for vertebral CT densitometry. J Comput Assist Tomogr 8(6):1164–1167
15. Kelcz F, Joseph PM, Hilal SK (1979) Noise considerations in dual energy CT scanning. Med Phys 6(5):418–425
16. Primak AN, Fletcher JG, Vrtiska TJ et al (2007) Noninvasive differentiation of uric acid versus non-uric acid kidney stones using dual-energy CT. Acad Radiol 14(12):1441–1447
17. Scheffel H, Stolzmann P, Frauenfelder T et al (2007) Dual-energy contrast-enhanced computed tomography for the detection of urinary stone disease. Invest Radiol 42(12):823–829
18. Graser A, Johnson TR, Bader M et al (2008) Dual energy CT characterization of urinary calculi: initial in vitro and clinical experience. Invest Radiol 43 (2):112–119
19. Sun C, Miao F, Wang XM et al (2008) An initial qualitative study of dual-energy CT in the knee ligaments. Surg Radiol Anat 30(5):443–447
20. Pozzi-Mucelli F, Bruni S, Doddi M et al (2007) Detection of intracranial aneurysms with 64 channel multidetector row computed tomography: comparison with digital subtraction angiography. Eur J Radiol 64(1):15–26
21. Gorzer H, Heimberger K, Schindler E (1994) Spiral CT angiography with digital subtraction of extra- and intracranial vessels. J Comput Assist Tomogr 18(5):839–841
22. Hoit DA, Malek AM (2006) Fusion of three-dimensional calcium rendering with rotational angiography to guide the treatment of a giant intracranial aneurysm: technical case report. Neurosurgery 58(1 Suppl):173–174
23. Nguyen-Huynh MN, Wintermark M, English J et al (2008) How accurate is CT angiography in evaluating intracranial atherosclerotic disease? Stroke 39 (4):1184–1188
24. Bash S, Villablanca JP, Jahan R et al (2005) Intracranial vascular stenosis and occlusive disease: evaluation with CT angiography, MR angiography, and digital subtraction angiography. AJNR Am J Neuroradiol 26(5):1012–1021

Eur Radiol (2009) 19: 2060–2065
DOI 10.1007/s00330-009-1358-x

NEURO

Kensuke Uotani
Yoshiyuki Watanabe
Masahiro Higashi
Tetsuro Nakazawa
Atsushi K. Kono
Yoshiro Hori
Tetsuya Fukuda
Suzu Kanzaki
Naoaki Yamada
Toshihide Itoh
Kazuro Sugimura
Hiroaki Naito

# Dual-energy CT head bone and hard plaque removal for quantification of calcified carotid stenosis: utility and comparison with digital subtraction angiography

Received: 27 August 2008
Revised: 24 November 2008
Accepted: 7 January 2009
Published online: 11 March 2009


K. Uotani · Y. Watanabe · M. Higashi · T. Nakazawa · A. K. Kono · Y. Hori · T. Fukuda · S. Kanzaki · N. Yamada · H. Naito
Department of Radiology,
National Cardiovascular Center,
Suita, Osaka, Japan

K. Uotani · K. Sugimura
Department of Radiology,
Kobe University Graduate
School of Medicine,
Kobe, Hyogo, Japan

T. Itoh
Siemens Asahi Medical Technologies,
Tokyo, Japan

K. Uotani (✉)
7-5-2 Kusuhoki-cho, Chuo-ku, Kobe,
Hyogo, 650-0017, Japan
e-mail: uota2@med.kobe-u.ac.jp
Tel.: +81-78-382-6104
Fax: +81-78-382-6129

**Abstract** We evaluated quantification of calcified carotid stenosis by dual-energy (DE) CTA and dual-energy head bone and hard plaque removal (DE hard plaque removal) and compared the results to those of digital subtraction angiography (DSA). Eighteen vessels (13 patients) with densely calcified carotid stenosis were examined by dual-source CT in the dual-energy mode (tube voltages 140 kV and 80 kV). Head bone and hard plaques were removed from the dual-energy images by using commercial software. Carotid stenosis was quantified according to NASCET criteria on MIP images and DSA images at the same plane. Correlation between DE CTA and DSA was determined by cross tabulation. Accuracies for stenosis detection and grading were calculated. Stenosis could be evaluated in all vessels by DE CTA after applying DE hard plaque removal. In contrast, conventional CTA failed to show stenosis in 13 out of 18 vessels due to overlapping hard plaque. Good correlation between DE plaque removal images and DSA images was observed ($r^2$=0.9504) for stenosis grading. Sensitivity and specificity to detect hemodynamically relevant (>70%) stenosis was 100% and 92%, respectively. Dual-energy head bone and hard plaque removal is a promising tool for the evaluation of densely calcified carotid stenosis.

**Keywords** Dual-source CT · Carotid stenosis · Dual-energy CT · Carotid plaque · CTA

## Introduction

Recent clinical trials have proven that the degree of the internal carotid artery stenosis is associated with cerebral stroke. According to the North American Symptomatic Carotid Endarterectomy Trial (NASCET) and the European Carotid Surgery Trial, symptomatic patients with severe stenoses (70–99%) can therefore benefit from carotid endarterectomy [1–3].

Conventional digital subtraction angiography (DSA) has been the "gold standard" for the evaluation of the degree of carotid artery stenosis, but conventional DSA has a tendency to underestimate the degree of carotid artery stenosis because it uses a limited number of projections and can therefore fail to detect the maximum internal carotid artery stenosis. 3D evaluation of carotid stenosis has become possible with rotation angiography, but this method remains invasive and is still associated with catheter-related complications.

Recently, noninvasive MR angiography (MRA) and CT angiography (CTA) have partially replaced conventional angiography [4–9] in particular since CTA correlates well

with catheter angiography and has high diagnostic accuracy for 70–99% stenosis. Moreover, high-quality DSA-like images can be generated with 3D CTA and maximum intensity projection (MIP) technique to gain an overview of the target vessel, which can help to detect maximum carotid stenosis. Nevertheless, CTA still shows a lower sensitivity for quantifying stenosis in the presence of dense calcification or indwelling stents since these may obscure contrast material in the lumen [10].

With dual-energy dual-source CT, two images can be simultaneously acquired with different tube voltages, corresponding to different X-ray energies. Materials can then be differentiated by analyzing their attenuation differences depending on tube voltage. The attenuation difference between two X-ray energies is especially large in materials with high atomic numbers such as iodine due to the photo effect, thus bones and calcified plaques, which show a smaller attenuation difference, can be distinguished from iodine [11, 12]. As a result, calcified plaque (hard plaque) can be removed from vessels with iodine contrast together with bone removal and quantification of carotid stenosis even in the presence of dense calcifications may become possible.

Here, we compared dual-energy head bone and hard plaque removal (DE hard plaque removal), applied to dual-energy CTA images, with conventional digital subtraction angiography (DSA) with a focus on quantification of calcified carotid artery stenosis.

## Materials and methods

This study was performed after approval of the local institutional review board. Written informed consent was obtained from all patients. In the period between June 2007 and December 2007, 16 patients with internal carotid artery stenosis underwent both carotid DSA and carotid CTA by using dual-source CT with dual-energy mode. Calcium volume was calculated on precontrast images by using a workstation (Zio M900 Quadra, Ziosoft, Japan). Patients with noncalcified or slightly calcified carotid stenosis (calcium volume$\leq$50 mm$^3$) were excluded. Finally, 13 patients with densely calcified carotid stenosis (calcium volume>50 mm$^3$) were enrolled and a total of 18 vessels were analyzed. CT angiography was performed using a dual-source multidetector CT system (SOMATOM Definition, Siemens, Germany). The dual-energy mode was operated with the following CT parameters: tube voltages of 140 kV and 80 kV, tube current–time products of 90 effective mA s and 380 effective mA s, respectively, a rotation time of 0.5 s per rotation, 64×0.6-mm collimation with z-flying focal spot and a pitch of 0.6. The contrast bolus was chosen according to the patients' body weight as 1 ml/kg of contrast material (350 mg I/ml) and injected for 20 s via the antecubital vein followed by 25 ml of saline. The delay before CT acquisition after injection was determined using bolus tracking software with a region of interest (ROI) was placed in a common carotid artery and a trigger threshold of 100 HU above the baseline. Two image datasets of different kV were reconstructed with 0.6-mm slice thickness and 0.6-mm slice gap. The reconstructed field of view was 200 mm. A soft convolution kernel (D30 kernel) was applied to obtain smooth 3D images. Dual-energy images of the carotids without bone and hard plaques were obtained from both datasets scanned at different tube voltage (Figs. 1 and 2) by using commercial postprocessing software (syngo 2008G, Siemens, Germany). We used the postprocessing software's default settings to remove cranial bone (head-bone removal). The combined images of both energy datasets were used for diagnostic reading and for 3D image (conventional CTA).

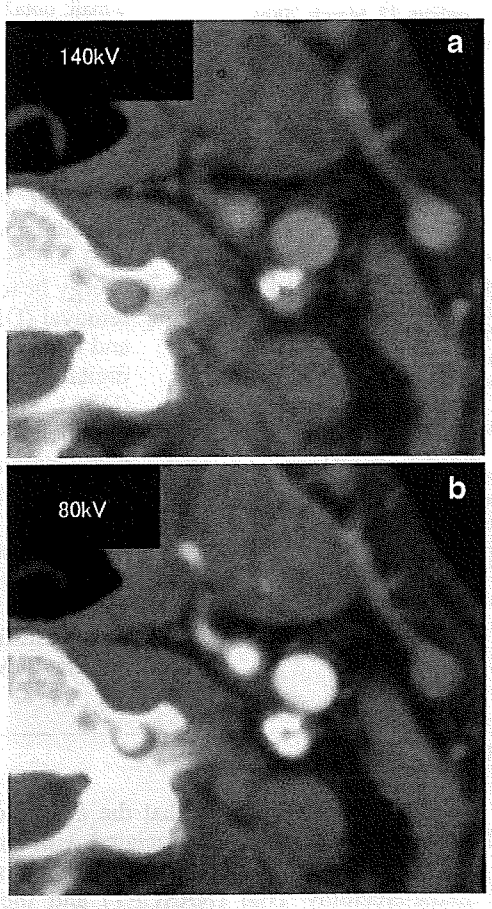


**Fig. 1** Two images acquired by DSCT in the dual-energy mode at different tube voltages (140 kV and 80 kV) displayed with the same window width and window center (WW=600, WL=200). The densities of iodine and calcifications are higher in the 80-kV than in the 140-kV images, but the density difference of iodine between the 80-kV and 140-kV images is higher than that of calcifications